

# Stellar hydrodynamical modeling of dwarf galaxies: simulation methodology, tests, and first results

Eduard I. Vorobyov<sup>1,2</sup>, Simone Recchi<sup>1</sup>, and Gerhard Hensler<sup>1</sup>

<sup>1</sup> Institute for Astrophysics, University of Vienna, Türkenschanzstrasse 17, Vienna 1180, Austria

<sup>2</sup> Research Institute of Physics, Southern Federal University, Stachki 194, Rostov-on-Don, Russia

Preprint online version: March 2, 2024

## ABSTRACT

**Context.** In spite of enormous progress and brilliant achievements in cosmological simulations, they still lack numerical resolution or physical processes to simulate dwarf galaxies in sufficient details. Accurate numerical simulations of individual dwarf galaxies are thus still in demand.

**Aims.** We aim at improving available numerical techniques to simulate individual dwarf galaxies. In particular, we aim at (i) studying in detail the coupling between stars and gas in a galaxy, exploiting the so-called stellar hydrodynamical approach, and (ii) studying for the first time the chemo-dynamical evolution of individual galaxies starting from self-consistently calculated initial gas distributions.

**Methods.** We present a novel chemo-dynamical code for studying the evolution of individual dwarf galaxies. In this code, the dynamics of gas is computed using the usual hydrodynamics equations, while the dynamics of stars is described by the stellar hydrodynamics approach, which solves for the first three moments of the collisionless Boltzmann equation. The feedback from stellar winds and dying stars is followed in detail. In particular, a novel and detailed approach has been developed to trace the aging of various stellar populations, which enables an accurate calculation of the stellar feedback depending on the stellar age. The code has been accurately benchmarked, allowing us to provide a recipe for improving the code performance on the Sedov test problem.

**Results.** We build initial equilibrium models of dwarf galaxies that take gas self-gravity into account and present different levels of rotational support. Models with high rotational support (and hence high degrees of flattening) develop prominent bipolar outflows; a newly-born stellar population in these models is preferentially concentrated to the galactic midplane. Models with little rotational support blow away a large fraction of the gas and the resulting stellar distribution is extended and diffuse. Models that start from non-self-gravitating initial equilibrium configurations, evolve at a much slower pace owing to lower initial gas density and hence lower star formation rate. The stellar dynamics turns out to be a crucial aspect of galaxy evolution. If we artificially suppress stellar dynamics, supernova explosions occur in a medium heated and diluted by the previous activity of stellar winds, thus artificially enhancing the stellar feedback.

**Conclusions.** The stellar hydrodynamics approach presents a promising tool for studying numerically the coupled evolution of gas and stars in dwarf galaxies.

**Key words.** Galaxies: abundances – Galaxies: dwarf – Galaxies: evolution – Galaxies: ISM – Galaxies: kinematics and dynamics

## 1. Introduction

Cosmological simulations are reaching nowadays extraordinary levels of complexity and sophistication. Based on the so-called standard model of cosmology (SMoC), these state-of-the-art simulations are able to reproduce the main features of observed large galaxies (see e.g. Brook et al., 2012; Zemp et al., 2012; Hopkins et al., 2013; Vogelsberger et al., 2014; Perret et al., 2014; Schaye et al., 2014), although severe disagreements with observations still persist (see e.g. Genel et al., 2014). However, the resolution of these simulations still does not allow to treat small-scale physics in dwarf galaxies (DGs).

Unfortunately, most of the weaknesses and problems shown by the SMoC manifest themselves in the range of masses typical for DGs (see e.g. Kroupa, 2012; Famaey & McGaugh, 2012, 2013, for recent reviews). Besides full-blown cosmological simulations, it is thus necessary to run simulations of individual galaxies or small groups of galaxies. This enables studying physi-

cal processes in more numerical resolution and address the problems of the SMoC. The simulation of individual galaxies is therefore still extremely relevant. Also in this field very remarkable level of accuracy have been reached (see e.g. Hopkins et al., 2013; Renaud et al., 2013; Roškar et al., 2013; Minchev et al., 2013; Teyssier et al., 2013, among others). The simulation of individual galaxies can also be used to parameterise feedback effects that can not be treated in detail in cosmological simulations (Creasey et al., 2013; Recchi, 2014).

An obvious drawback of simulating individual galaxies is that it is not clear what initial conditions one should adopt. A common strategy is to consider a rotating, isothermal gas in equilibrium with the potential generated by a fixed distribution of stars and/or of dark matter (DM), but not with the potential generated by the gas itself (Tomisaka & Ikeuchi, 1988; Silich & Tenorio-Tagle, 1998; Mac-Low & Ferrara, 1999; Recchi & Hensler, 2013). A typical justification for neglecting gas self-gravity in DG sim-

ulations is that the mass budget of these objects should be dominated by dark matter. In our previous paper (Vorobyov et al., 2012), we have explained in detail why this approach may produce unrealistic initial gas distributions and considered also the gas self-gravity when building equilibrium initial conditions.

As known from stellar structure studies (see e.g. Ostriker & Mark, 1968), the inclusion of gas self-gravity leads to implicit equations describing the initial equilibrium configuration, which must be solved iteratively. We have done that for different halo masses, different degrees of rotational support and different initial temperatures and we have calculated the amount of gas prone to star formation for each of these models. Our star formation criteria were based on the Toomre instability criterium and on the Kennicutt-Schmidt empirical correlation between gas surface density and star formation rate (SFR) per unit area (see Vorobyov et al., 2012, for more details). For models that satisfy both star formation criteria, the underlying assumption was that the initial configuration is marginally stable to star formation and an external perturbing agent can trigger star formation in the corresponding parts of the galaxy.

The subsequent logical step is to use these marginally stable configurations as initial conditions for full-blown hydrodynamical simulations. For this purpose, we have developed a detailed 2+1 dimensional hydrodynamical code in cylindrical coordinates with assumed axial symmetry, which treats both the stellar and gaseous components as well as the phase transitions between them. Of course, a real galaxy may depart from such axial symmetry. However, since our initial conditions are axially symmetric and we do not explicitly consider environmental effects in this paper, the departures from axial symmetry are not expected to be significant.

This is the first of a series of papers devoted to numerically studying DGs with self-consistent initial conditions. Here, we explain in detail the basic strategy and the employed numerical hydrodynamical methods, which we extensively benchmark. Furthermore, we run a few representative models to show the overall early evolution of a typical DG. We pay particular attention to the co-evolution of stars and gas in our simulations. We follow the motion of stars by means of the so-called stellar hydrodynamical approach (Theis et al., 1992; Samland et al., 1997; Vorobyov & Theis, 2006; Mitchell et al., 2013; Kulikov, 2014), according to which the stellar component of a galaxy can be treated as a fluid. We develop this approach further and describe how stars and gas can be coupled by means of star formation and stellar feedback processes.

The paper is organised as follows. In section 2 we describe the simulation methodology, paying specific attention to coupling the stars and gas via star formation and stellar feedback. Section 3 contains the gas cooling and heating rates employed in our modeling. The solution method of our stellar hydrodynamics equations is described in Section 4. The evolution of several representative models of DGs is studied in Section 5. Model caveats are discussed in Section 6. The main conclusions are summarized in Section 7 and we benchmark our code against a suite of test problems in the Appendix.

## 2. Simulation methodology

Our model DGs consist of a gas disk, stellar component, and fixed dark matter halo. The gas disk is a mixture of nine chemical elements (H, He, C, O, N, Ne, Mg, Si, and Fe), with the initial abundance of heavy elements set by the adopted initial metallicity. The stellar component consists of new stars born in the course of numerical simulations and has no pre-existing component. The DM halo has a spherically symmetric form and contributes only to the total gravitational potential of the system.

We describe the time evolution of our model galaxies using the coupled system of gas and stellar hydrodynamics equations complemented with phase transformations between stars and gas, chemical enrichment by supernova explosions, low- and intermediate-mass stars and also star formation feedback. We assume that individual chemical elements are well coupled dynamically with the bulk motion of the gas, which means that we need to solve only for the continuity equation for every chemical element with mass density  $\rho_i$  and need not to solve for the dynamics of every element separately. Below, we provide a brief explanation for the key equations used to evolve our system in time.

### 2.1. Gas hydrodynamics

The dynamics of gas is modelled using the usual hydrodynamics equations for the gas density of  $\rho_g$ , momentum  $\rho_g \mathbf{v}_g$ , and internal energy density  $\epsilon$  complemented with the rates of mass, momentum and energy transfer between the gas and stellar components and also with the continuity equations for the mass density of every chemical element  $\rho_i$

$$\frac{\partial \rho_g}{\partial t} + \nabla \cdot (\rho_g \mathbf{v}_g) = \mathcal{S} - \mathcal{D}, \quad (1)$$

$$\frac{\partial \rho_i}{\partial t} + \nabla \cdot (\rho_i \mathbf{v}_g) = \mathcal{S}^i - \mathcal{D}^i, \quad (2)$$

$$\frac{\partial}{\partial t} (\rho_g \mathbf{v}_g) + \nabla \cdot (\rho_g \mathbf{v}_g \otimes \mathbf{v}_g) = -\nabla P + \rho_g \mathbf{g}_{\text{gr}} + \mathbf{v}_s \mathcal{S} - \mathbf{v}_g \mathcal{D}, \quad (3)$$

$$\frac{\partial \epsilon}{\partial t} + \nabla \cdot (\epsilon \mathbf{v}_g) = -P \nabla \cdot \mathbf{v}_g - \Lambda + \Gamma + \Gamma_* - \epsilon \frac{\mathcal{D}}{\rho_g}. \quad (4)$$

Here,  $\mathbf{v}_g$  and  $\mathbf{v}_s$  are the gas and stellar velocities,  $P = (\gamma - 1)\epsilon$  is the gas pressure linked to the internal energy density via the ideal equation of state with the ratio of specific heats  $\gamma = 5/3$  and  $\mathbf{g}_{\text{gr}}$  is the gravitational acceleration due to gas, stars, and DM halo. The gas cooling  $\Lambda$  due to line and continuum emission and gas heating  $\Gamma$  due to cosmic rays and small dust grains are explained in detail in Section 3. The gas heating due to stellar feedback  $\Gamma_*$  is calculated as the sum of the contributions from SNII and SNIa explosions ( $\Gamma_{\text{SNII}}$  and  $\Gamma_{\text{SNIa}}$ , respectively), and also from the stellar winds  $\Gamma_{\text{sw}}$ . The last term on the r.h.s. of equation (4) accounts for the decrease in the internal energy due to formation of stars from the gas phase. We note that the quantity  $\rho_g \mathbf{v}_g \otimes \mathbf{v}_g$  is the symmetric dyadic (a rank-two tensor) calculated according to the usual rules and  $\nabla \cdot (\rho_g \mathbf{v}_g \otimes \mathbf{v}_g)$  is the divergence of a rank-two tensor.

The source term  $\mathcal{S}$  denotes the phase transformation of stars into the gas phase and is defined as the sum of

the mass release rates (per unit volume) of all individual elements,  $\mathcal{S} = \sum_i \mathcal{S}_i$ . The mass release rate of a particular element  $i$  is defined as

$$\mathcal{S}^i = \mathcal{S}_{\text{SNII}}^i + \mathcal{S}_{\text{SNIa}}^i + \mathcal{S}_*^i, \quad (5)$$

where  $\mathcal{S}_{\text{SNII}}^i$ ,  $\mathcal{S}_{\text{SNIa}}^i$ , and  $\mathcal{S}_*^i$  are the contributions due to SNII, SNIa, and also due to low- and intermediate mass stars, respectively. The sink term  $\mathcal{D}$  describes the phase transformation of gas into stars according to the adopted star formation law. The detailed explanation of all relevant rates is provided in Section 2.7.

## 2.2. Stellar hydrodynamics

The time evolution of the stellar component is computed using the Boltzmann moment equation approach introduced by Burkert & Hensler (1988) and further developed in application to stellar disks in Samland et al. (1997) and Vorobyov & Theis (2006). In this approach, the dynamics of stars is described by the first three moments of the collisionless Boltzmann moment equations

$$\frac{\partial \rho_s}{\partial t} + \nabla \cdot (\rho_s \mathbf{v}_s) = \mathcal{D} - \mathcal{S}, \quad (6)$$

$$\begin{aligned} \frac{\partial}{\partial t} (\rho_s \mathbf{v}_s) + \nabla \cdot (\mathbf{v}_s \otimes \rho_s \mathbf{v}_s) = & -\nabla \cdot \Pi + \rho_s g_{\text{gr}} - \\ & - \mathbf{v}_s \mathcal{S} + \mathbf{v}_g \mathcal{D}, \end{aligned} \quad (7)$$

$$\begin{aligned} \frac{\partial \Pi_{ij}}{\partial t} + \nabla \cdot (\Pi_{ij} \mathbf{v}_s) = & -\Pi_{ik} : (\nabla \mathbf{v}_s)_{jk} - \Pi_{jk} : (\nabla \mathbf{v}_s)_{ik} - \\ & - \sigma_{ij}^2 \mathcal{S} + \sigma_*^2 \mathcal{D}, \end{aligned} \quad (8)$$

where  $\rho_s = m \int f d^3 \mathbf{u}$  is the stellar mass density,  $\mathbf{v}_s = \rho_s^{-1} m \int f \mathbf{u} d^3 \mathbf{u}$  is the mean stellar velocity, and  $\Pi$  is the stress tensor with six components  $\Pi_{ij} \equiv \rho_s \sigma_{ij}^2$ . The stellar velocity dispersions are defined as  $\sigma_{ij}^2 = \rho^{-1} m \int f (u_i - v_i)(u_j - v_j) d^3 \mathbf{u}$ . The function  $f$  is the distribution function of stars in the six dimensional position-velocity phase space  $f \equiv f(t, \mathbf{x}, \mathbf{u})$  and  $m$  is the average mass of a star. The quantity  $\nabla \mathbf{v}_s$  is the gradient of a vector, the covariant expression for which is provided, e.g., in Stone & Norman (1992) and  $\Pi_{ik} : (\nabla \mathbf{v}_s)_{jk}$  is the convolution (over index  $k$ ) of two rank-two tensors. The quantity  $\sigma_*$  represents a typical stellar velocity dispersion of a new-born cluster of stars, for which we take a fiducial value of  $5.0 \text{ km s}^{-1}$ .

## 2.3. Massive stars

Massive stars that end up their life with SNII explosions are main contributors to the energy budget and chemical composition of the interstellar medium. Therefore, it is important to follow their evolution as accurate as possible. We improve the description of the stellar component by solving for a separate continuity equation for the mass volume density  $\rho_s^h$  of stars with mass  $> 8.0 M_\odot$

$$\frac{\partial \rho_s^h}{\partial t} + \nabla \cdot (\rho_s^h \mathbf{v}_s) = f_h \mathcal{D} - \mathcal{S}^h, \quad (9)$$

where  $f_h$  is the fraction of stars with mass  $> 8.0 M_\odot$  calculated according to the adopted IMF (see equation 14) and

$\mathcal{S}_h$  is the rate of death of massive stars. The massive star subcomponent has the same dynamical properties as the rest of the stars, an assumption that we plan to relax in the future.

## 2.4. Intermediate-mass stars

Stars in the  $(1.0 - 8.0) M_\odot$  mass range produce the majority of carbon and nitrogen. Moreover, binary stars in this mass range can explode as Type Ia supernovae and are thus important sources of iron. Therefore, we also solve for a separate continuity equation for the mass volume density  $\rho_s^m$  of intermediate-mass stars

$$\frac{\partial \rho_s^m}{\partial t} + \nabla \cdot (\rho_s^m \mathbf{v}_s) = f_m \mathcal{D} - \mathcal{S}^m, \quad (10)$$

where  $f_m$  is the fraction of stars with mass  $1.0 M_\odot < m < 8.0 M_\odot$  calculated according to the adopted IMF and  $\mathcal{S}_m$  is the rate of death of intermediate-mass stars. We note that the stellar evolution of low-mass stars can be neglected during the galactic evolution. They only contribute to the gravitational potential where their density can be deduced from  $\rho_s$  (the total stellar density),  $\rho_s^h$ , and  $\rho_s^m$ .

## 2.5. Gravity of gas, stars, and DM halo

The gravitational potential of gas and stars is calculated self-consistently by solving for the Poisson equation

$$\nabla^2 \Phi_{g+s} = 4\pi G (\rho_g + \rho_s). \quad (11)$$

To accelerate the simulations, we solve for Equation (11) only when the relative error in the currently stored gravitational potential compared to the current density distribution exceeds  $10^{-5}$  (see Stone & Norman, 1992, for details).

The gravitational acceleration due to a spherically symmetric DM halo  $\mathbf{g}_h$  is calculated as explained in Vorobyov et al. (2012). Two options are available in the code: a cored isothermal DM halo profile and a Navarro-Frenk-White (or cuspy) profile. In this paper, we use the cored isothermal DM profile. The total gravitational acceleration is calculated as  $\mathbf{g}_{\text{gr}} = \mathbf{g}_h - \nabla \Phi_{g+s}$ .

## 2.6. Mean stellar age

In order to calculate the mass and energy release rates by supernovae and dying low-mass stars one needs to know the age of stars. In the stellar hydrodynamics approach, stars are a mixture of populations with different ages. Nevertheless, one may define the mean age of stars  $\bar{\tau}_*$ , which should obey the following rules:

1. The bulk motion of stars, such as compression or rarefaction, should not affect the value of  $\bar{\tau}_*$ . This can be achieved by solving for the Lagrangian or comoving equation for  $\bar{\tau}_*$

$$\frac{d\bar{\tau}_*}{dt} \equiv \frac{\partial \bar{\tau}_*}{\partial t} + (\mathbf{v}_s \cdot \nabla) \bar{\tau}_* = 0 \quad (12)$$

2. A newly-born stellar population should rejuvenate the pre-existing one. This is achieved by updating the mean age every timestep in every grid cell using the following equation

$$\bar{\tau}_*^{\text{rv}} = \frac{M_s \bar{\tau}_* + \Delta M_s \Delta t}{M_s + \Delta M_s}, \quad (13)$$

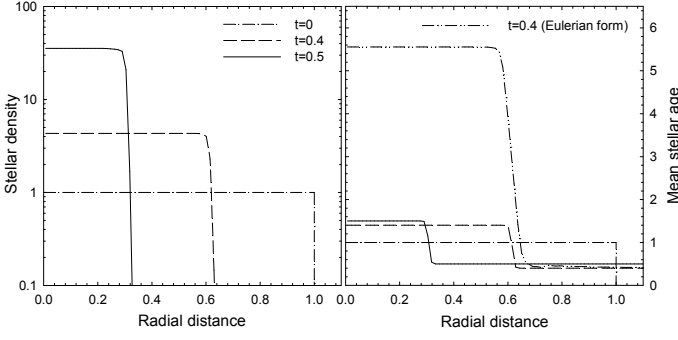


**Fig. 1.** Star volume density (left) and mean stellar age (right) as a function of time during the gravitational collapse of a stellar sphere of unit radius. The elapsed time is indicated in the left panel. Star formation is turned off for this test problem. The dash-dot-dotted lines shows the mean stellar age when calculated using the Eulerian form to account for bulk motions of stars instead of the Lagrangian form (see text for more detail.)

where  $M_s$  is the stellar mass in a specific cell and  $\Delta M_s$  the mass of stars born in the same cell during timestep  $\Delta t$ . Equation (13) satisfies the expected asymptotic behaviour of the stellar age, which becomes small ( $\bar{\tau}_*^{\text{riv}} \rightarrow \Delta t$ ) during a massive instantaneous burst ( $\Delta M_s \rightarrow \infty$ ), but remains almost unchanged ( $\bar{\tau}_*^{\text{riv}} \rightarrow \bar{\tau}_*$ ) in the quiescent phase  $\Delta M_s \rightarrow 0$ .

3. The mean stellar age should uniformly increase with time, reflecting the overall aging of the system. This is done by adding the current timestep  $\Delta t$  to the mean stellar age in every grid cell. Thus, in the absence of star formation and pre-existing old stellar population, the mean stellar age is equivalent to the current evolution time  $t$ .

In practice, we first solve for Equation (12) to account for bulk motions, then we update the mean stellar age in every grid cell according to Equation (13) to account for star formation, and finally we add the current timestep  $\Delta t$  to the mean stellar age in every grid cell to take into account the aging of stellar populations. Since we follow the evolution of both the massive and intermediate-mass star subcomponents, their mean ages  $\bar{\tau}_*^h$  and  $\bar{\tau}_*^m$ , respectively, need to be calculated using the same procedure.

Figure 1 shows the time evolution of the stellar density  $\rho_s$  (left panel) and mean stellar age  $\bar{\tau}_*$  (right panel) in an idealized test problem involving the gravitational collapse of a stellar sphere with unit radius. Initially,  $\rho_s$  and  $\bar{\tau}_*$  are set to unity inside the sphere and to zero outside the sphere (dash-dotted lines). The stellar velocity dispersion is negligible everywhere and the star formation rate is set to zero. As the collapse proceeds, stellar density shows the expected behaviour with a central plateau shrinking in size and growing in density. At the same time the mean stellar age increases in concordance with time, as expected in the absence of star formation. In particular, the difference between the values of  $\bar{\tau}_*$  inside and outside the sphere is always equal to unity, as was set initially. We emphasize here the need for using the Lagrangian equation for  $\bar{\tau}_*$ . If the Eulerian form  $\partial \bar{\tau}_* / \partial t + \nabla \cdot (\mathbf{v}_s \bar{\tau}_*) = 0$  is used instead, the above test fails. Indeed, the dash-dot-dotted line shows the mean stellar age at  $t = 0.4$  calculated using the Eulerian form. Evidently, the difference between the values of  $\bar{\tau}_*$  in-

side and outside the sphere is now much greater than unity, indicating a spurious aging of the stellar populations inside the sphere<sup>1</sup>.

Finally, we note that the concept of the mean stellar age has its limitations. For instance, in the case of a constant SFR and steady galaxy configuration,  $\bar{\tau}_*^h$  approaches a constant value after a few tens of Myr, meaning that the supernova rates and mass return rates (see equations (17) and (19)) will be exclusively determined by stars whose lifetime is equal to  $\bar{\tau}_*^h$ . This bias towards stars with single age (and mass) diminishes, when a time-varying SFR is present or stellar motions are taken into account. Nevertheless, a more sophisticated approach that takes into account a possible age spread around the mean value is desirable.

## 2.7. Source and sink terms

In order to calculate the rates at which stars return their mass (including newly synthesized elements) into the gas phase, we need to make assumptions about the initial mass function (IMF), stellar lifetimes and nucleosynthesis rates.

We adopt the Kroupa IMF (Kroupa, 2001) of the form

$$\phi(M_*) = \begin{cases} A M_*^{-1.3} & \text{if } M_* \leq 0.5 M_\odot \\ B M_*^{-2.3} & \text{if } M_* > 0.5 M_\odot \end{cases}, \quad (14)$$

where the normalization constants  $A$  and  $B$  are calculated as described in Sections 2.7.1 and 2.7.2.

The stellar lifetimes are taken from Padovani & Matteucci (1993)

$$\tau(M_*) = \begin{cases} 1.2 M_*^{-1.85} + 0.003 \text{ Gyr} & \text{if } M_* \geq 7.45 M_\odot \\ 10^{f(M_*)} \text{ Gyr} & \text{if } M_* < 7.45 M_\odot \end{cases}, \quad (15)$$

where

$$f(M_*) = \frac{\{0.334 - \sqrt{1.79 - 0.2232 \times (7.764 - \log(M_*))}\}}{0.1116}. \quad (16)$$

In equation (15), we have adjusted the transitional value for the stellar mass ( $7.45 M_\odot$ ) in order to obtain a smooth time derivative  $dM_*/d\tau$ .

### 2.7.1. Supernova type II rates

We assume that all stars in the  $[8.0 M_\odot : M_*^{\text{max}}]$  mass range end their life cycle as type II supernovae (SNeII), where  $M_*^{\text{max}}$  is the upper cut-off mass of the IMF set to  $100 M_\odot$  in our model. The SNeII rate, i.e., the number of SNeII per unit time, is then defined as

$$\mathcal{R}_{\text{SNeII}} = \begin{cases} \phi[M_*(\bar{\tau}_*^h)] \frac{dM_*(\bar{\tau}_*^h)}{d\tau} & \text{if } \bar{\tau}_*^h \in [\tau(100 M_\odot) : \tau(8.0 M_\odot)], \\ 0 & \text{if } \bar{\tau}_*^h \ni [\tau(100 M_\odot) : \tau(8.0 M_\odot)], \end{cases} \quad (17)$$

where  $M_*(\bar{\tau}_*^h)$  is the mass of a massive star that is about to die as SNeII calculated by inverting equation (15). This is the SNeII rate following an instantaneous burst of star formation. We therefore assume here that each star formation event generates a single stellar population (SSP). The

<sup>1</sup> It is still possible to use the Eulerian form for the product  $\rho_s \bar{\tau}_*$  instead of just  $\bar{\tau}_*$ . We leave the exact derivation of the pertinent equations for a followup study.



superposition of SNII rates coming from many SSPs will then approximate the SNII rate in the presence of a variable SFR. The derivative  $dM_*/d\tau$  is calculated by inverting equation (15) and then differentiating it with respect to time.

The IMF in equation (17) has to be normalized according to the total mass of massive stars  $M_{s,\text{tot}}^h$  in each computational cell

$$\int_{8.0 M_\odot}^{M_*(\bar{\tau}_*^h)} \phi(M_*) M_* dM_* = M_{s,\text{tot}}^h. \quad (18)$$

We note that the upper limit in the integral is not fixed but rather depends on the mean stellar age of massive stars in a given computational cell. This is done to take into account the fact that massive stars with lifetimes smaller than  $\bar{\tau}_*^h$ , and hence with mass greater than  $M_*(\bar{\tau}_*^h)$ , must have exploded as SNeII. Excluding those stars ensures a correct calculation of the stellar mass spectrum at any time instant<sup>2</sup>. Since  $M_s^h$  and  $M_*(\bar{\tau}_*^h)$  are time-varying quantities, the normalization constants in the IMF need to be updated every time step.

The mass return rate (per unit volume) by SNII explosions can now be defined as

$$\mathcal{S}_{\text{SNII}}^i = \mathcal{R}_{\text{SNII}} \rho_{\text{SNII}}^i[M_*(\bar{\tau}_*^h)], \quad (19)$$

where  $\rho_{\text{SNII}}^i[M_*(\bar{\tau}_*^h)]$  is the mass (per unit volume) released by a SNII of mass  $M_*$  in the form of a specific element  $i$ . The values of  $\rho^i$  for nine considered elements (H, He, C, O, N, Ne, Mg, Si, and Fe) and four stellar metallicities ( $Z_* = 10^{-4}, 10^{-2}, 10^{-1}$ , and 1.0 times solar) are taken from Woosley & Weaver (1995). For stellar masses greater than  $40 M_\odot$ , the yields are set constant to those of a  $40 M_\odot$  star.

Finally, we assume that each supernova releases  $\epsilon_{\text{SN}} \times 10^{51}$  ergs in the form of thermal energy and define the rate of energy density released by SNeII as

$$\Gamma_{\text{SNII}} = 10^{51} \epsilon_{\text{SN}} \mathcal{R}_{\text{SNII}} V^{-1}, \quad (20)$$

where  $V$  is the injection volume specified by the actual size of our numerical grid and  $\epsilon_{\text{SN}}$  is the ejection efficiency set to 1.0 in this work (see Section 6 for discussion.).

### 2.7.2. Supernova type Ia rates

We derive the rates of Type Ia supernovae following the ideas and notations laid out in Matteucci & Recchi (2001). The number of binary systems (per unit mass of the binary system  $M_B$ ) that are capable of producing a SNIa explosion can be calculated as

$$N_{\text{SNIa}}[M_2(\bar{\tau}_*^m)] = A_* \int_{M_{B,1}}^{M_{B,2}} \phi(M_B) f\left(\frac{M_2(\bar{\tau}_*^m)}{M_B}\right) \frac{dM_B}{M_B}, \quad (21)$$

where  $M_2(\bar{\tau}_*^m)$  is the mass of the secondary component,  $A_*$  a normalization constant and the limits of the integral are

<sup>2</sup>  $M_*(\bar{\tau}_*^h)$  should depend on  $M_{s,\text{tot}}^h$  because small stellar populations, characterized by a small amount of massive stars, could have an IMF truncated at relatively low masses (Ploekinger et al., 2014). We neglect this effect in this paper.

defined as

$$M_{B,1} = \max[2M_2(\bar{\tau}_*^m), M_{B,\text{min}}] \quad (22)$$

$$M_{B,2} = \frac{1}{2} M_{B,\text{max}} + M_2(\bar{\tau}_*^m). \quad (23)$$

The maximum and minimum masses of a binary system that is capable of producing a SNIa explosion are set to  $M_{B,\text{min}} = 3.0 M_\odot$  and  $M_{B,\text{max}} = 16.0 M_\odot$ , respectively, and the maximum mass of the secondary is  $M_2 = 8.0 M_\odot$ . The quantity  $f(M_2(\bar{\tau}_*^m)/M_B)$  in equation (21) is the distribution function of the  $M_2(\bar{\tau}_*^m)/M_B$  ratio and is defined as

$$f\left(\frac{M_2(\bar{\tau}_*^m)}{M_B}\right) = 2^{1+\gamma} (1+\gamma) \left(\frac{M_2(\bar{\tau}_*^m)}{M_B}\right)^\gamma, \quad (24)$$

and  $\gamma$  is set to 0.5. For this value of  $\gamma$ , the normalization constant that better reproduces the observed  $[\alpha/\text{Fe}]$  ratios in dwarf galaxies is  $A_* = 0.06$  (Recchi et al., 2009), therefore we adopt this value in the present work.

By analogy to the massive star subcomponent, the IMF in equation (21) has to be normalized according to the total mass of intermediate-mass stars  $M_{s,\text{tot}}^m$  in each computational cell

$$\int_{1.0 M_\odot}^{M_*(\bar{\tau}_*^m)} \phi(M_*) M_* dM_* = M_{s,\text{tot}}^m. \quad (25)$$

The SNIa rate, i.e., the number of SNIa explosions per unit time, can now be calculated by analogy to equation (17) as

$$\mathcal{R}_{\text{SNIa}} = \begin{cases} N_{\text{SNIa}}[M_2(\bar{\tau}_*^m)] \frac{dM_2(\bar{\tau}_*^m)}{d\tau} & \text{if } \bar{\tau}_*^m \in [\tau(8.0 M_\odot) : \tau(M_{2,\text{min}})], \\ 0 & \text{if } \bar{\tau}_*^m \ni [\tau(8.0 M_\odot) : \tau(M_{2,\text{min}})], \end{cases} \quad (26)$$

where  $M_{2,\text{min}} = 1.0 M_\odot$  is the minimum mass of the secondary.

The mass return rate (per unit volume) by SNIa explosions can now be expressed as

$$\mathcal{S}_{\text{SNIa}}^i = \mathcal{R}_{\text{SNIa}} \rho_{\text{SNIa}}^i[M_*(\bar{\tau}_*^m)], \quad (27)$$

where  $\rho_{\text{SNIa}}^i[M_*(\bar{\tau}_*^m)]$  is the mass (per unit volume) released by a SNIa of mass  $M_*$  in the form of a specific element  $i$ . The values of  $\rho^i$  for six elements (C, O, N, Mg, Si, and Fe) are taken from Nomoto et al. (1984). We neglect the metallicity dependence of the SNIa yields. The energy release rate by SNIa ( $\Gamma_{\text{SNIa}}$ ) is defined in analogy to Equation (20), with  $\mathcal{R}_{\text{SNII}}$  being substituted by  $\mathcal{R}_{\text{SNIa}}$ .

### 2.7.3. Stellar winds and the mass return by intermediate-mass stars

The luminosity produced by stellar winds is taken from results of the Starburst99 software package (Leitherer et al., 1999; Vazquez & Leitherer, 2005). We used Padova AGB stellar tracks at different metallicities ( $Z_* = 0.0004, 0.004, 0.008, 0.02, 0.05$ ) and used this set of models as a library to obtain wind luminosities for each SSP, depending on its mass and average metallicity. The energy transfer efficiency of the wind power is set to 100%.

The mass-return rate (per unit volume) by winds of stars in the  $(1.0 - 8.0) M_\odot$  mass range is calculated as

$$S_*^i = \mathcal{R}_* \rho_*^i [M_*(\bar{\tau}_*^m)], \quad (28)$$

where the number of stars with mass  $1.0 < M_* < 8.0 M_\odot$  dying per unit time is expressed as

$$\mathcal{R}_* = \begin{cases} \phi[M_*(\bar{\tau}_*^m)] \frac{dM_*(\bar{\tau}_*^m)}{d\tau} & \text{if } t \in [\tau(8.0 M_\odot) : \tau(1.0 M_\odot)], \\ 0 & \text{if } t \notin [\tau(8.0 M_\odot) : \tau(1.0 M_\odot)], \end{cases} \quad (29)$$

and the mass (per unit volume) returned by dying stars  $\rho_*^i$  in the form of a specific element  $i$  includes both the true nucleosynthesis yields of C, O, and N and the pre-existed contribution (see Recchi et al., 2001). The nucleosynthesis yields are taken from van den Hoek & Groenewegen (1997).

#### 2.7.4. Star-formation rate

The phase transformation of gas into stars is controlled by the following SFR per unit volume

$$\mathcal{D} = \begin{cases} c_* \frac{(\rho_g \xi_{\text{cpw}})^{1.5}}{\max(\tau_{\text{ff}}, \tau_c)} \left[ \frac{T_0^2}{T_0^2 + T^2} \right]^2 & \text{if } n_g \geq n_{\text{cr}} \text{ and } \nabla \cdot \mathbf{v}_g < 0, \\ 0 & \text{if } n_g < n_{\text{cr}} \text{ or } \nabla \cdot \mathbf{v}_g > 0, \end{cases} \quad (30)$$

where  $n_g$  and  $T$  are the gas number density and temperature, respectively,  $\nabla \cdot \mathbf{v}_g$  is the gas velocity divergence, and  $\xi_{\text{cpw}}$  is the cold plus warm gas fraction (see Section 3.4 for detail). The exponent 1.5 in Equation (30) is expected if the SFR is proportional to the ratio of the local gas volume density to the free-fall time, and the free-fall and cooling times are calculated as  $\tau_{\text{ff}} = \sqrt{3\pi/(32G\rho_g)}$  and  $\tau_c = \epsilon/\Lambda$ , respectively<sup>3</sup>. The term in brackets applies the adopted temperature dependence by quickly turning off star formation at temperatures greater than  $T_0 = 10^3$  K. For consistency with other studies (e.g. Springel & Hernquist, 2003), the critical gas number density above which star formation is allowed is set to  $1.0 \text{ cm}^{-3}$  (see discussion in Section 6). Finally, the normalization constant  $c_*$  is set to 0.05 (Stinson et al., 2006).

#### 2.8. Stellar metallicity

The heavy element yields by SNeII and also by low- and intermediate-mass stars are metallicity dependent. We calculate the stellar metallicity  $Z_*$  using a procedure similar to that applied to the mean stellar age in Section 2.6. First, we solve for the Lagrangian equation for  $Z_*$  to account for bulk motions

$$\frac{dZ_*}{dt} \equiv \frac{\partial Z_*}{\partial t} + (\mathbf{v}_s \cdot \nabla) Z_* = 0. \quad (31)$$

Then, we update the stellar metallicity in every grid cell to account for the production of metals due to star formation using the following equation

$$Z_*^{\text{new}} = \frac{M_s Z_* + \Delta M_s Z_g}{M_s + \Delta M_s}, \quad (32)$$

<sup>3</sup> Strictly speaking, this is only true when  $\tau_c > \tau_{\text{ff}}$ . Otherwise, the density exponent should be set to 1.0.

where  $Z_g$  is the current metallicity of gas from which stars form. Equation (32) satisfies the expected asymptotic behaviour of the stellar metallicity, which approaches that of the gas ( $Z_*^{\text{new}} \rightarrow Z_g$ ) during a massive instantaneous burst ( $\Delta M_s \rightarrow \infty$ ), but remains almost unchanged ( $Z_*^{\text{new}} \rightarrow Z_*$ ) in the quiescent phase  $\Delta M_s \rightarrow 0$ . We note that step 3 from Section 2.6 needs not be applied to the stellar metallicity, because this step takes into account the overall aging of stellar populations.

### 3. Cooling and heating rates

We assume that the gas is in collisional ionization equilibrium and calculate the gas cooling rates using the cooling functions presented in Böhringer & Hensler (1989) and Dalgarno & McCray (1972).

#### 3.1. Low-temperature cooling

For the low-temperature cooling  $T < 10^4$  K, we adopted the cooling rates as described in Dalgarno & McCray (1972). The chemical elements that are taken into account are H, O, C, N, Si, and Fe. For high fractional ionization, cooling is mostly provided by collisions of neutral and singly-ionized ions with thermal electrons. We have assumed that most of oxygen and nitrogen is in neutral form. The following equations describe the cooling efficiency  $L_e(X_i)$  (in  $\text{erg cm}^3 \text{ s}^{-1}$ ) due to collisions of element  $X_i$  of number density  $n_i$  with thermal electrons of number density  $n_e$ .

$$L_e^{\text{low}}(\text{C}^+) = T^{-1/2} \left( 7.9 \times 10^{-20} e^{-92/T} + 3.0 \times 10^{-17} e^{-61900/T} \right), \quad (33)$$

$$L_e^{\text{low}}(\text{Si}^+) = T^{-1/2} \left( 1.9 \times 10^{-18} e^{-413/T} + 3.0 \times 10^{-17} e^{-63600/T} \right), \quad (34)$$

$$L_e^{\text{low}}(\text{Fe}^+) = T^{-1/2} \left( 4.8 \times 10^{-18} e^{-2694/T} + 1.1 \times 10^{-18} \left[ e^{-554/T} + 1.3e^{-961/T} \right] + 7.8 \times 10^{-18} e^{-3496/T} \right), \quad (35)$$

$$L_e^{\text{low}}(\text{O}) = 1.74 \times 10^{-24} T^{1/2} \times \left[ \left( 1 - 7.6T^{-1/2} \right) e^{-228/T} + 0.38 \left( 1 - 7.7T^{-1/2} \right) e^{-326/T} \right] + 9.4 \times 10^{-23} T^{1/2} e^{-22700/T}, \quad (36)$$

$$L_e^{\text{low}}(\text{N}) = 8.2 \times 10^{-22} T^{1/2} \times \left( 1 - 2.7 \times 10^{-9} T^2 \right) e^{-27700/T}. \quad (37)$$

The cooling rate per unit volume  $\Lambda^{\text{low}}$  ( $\text{erg cm}^{-3} \text{ s}^{-1}$ ) due to collisions of element  $X_i$  with thermal electrons is then calculated as  $L_e^{\text{low}}(X_i) n_i n_e$ . Cooling due to collisions of hydrogen atoms with thermal electrons, as tabulated in Table 2 of Dalgarno & McCray (1972) is also taken into account.

For low fractional ionization, collisions of  $\text{C}^+$ , O,  $\text{Si}^+$ , and  $\text{Fe}^+$  with neutral hydrogen may become important con-

tributors to the total cooling budget. The following equations describe the corresponding cooling efficiency for  $\text{Si}^+$  and  $\text{Fe}^+$ .

$$L_{\text{H}}^{\text{low}}(\text{Si}^+) = 7.4 \times 10^{-23} e^{-413/T}, \quad (38)$$

$$L_{\text{H}}^{\text{low}}(\text{Fe}^+) = 1.1 \times 10^{-22} \left( e^{-554/T} + 1.4e^{-961/T} \right). \quad (39)$$

The cooling rate per unit volume due to collisions of element  $X_i$  with hydrogen atoms of number density  $n_{\text{H}}$  is then calculated as  $L_{\text{H}}^{\text{low}}(X_i) n_i n_{\text{H}}$ . The cooling efficiencies due to collisions of O and C<sup>+</sup> with neutral hydrogen are taken from Table 4 of Dalgarno & McCray (1972).

To summarize, the total cooling rate at the low-temperature regime is calculated as

$$\Lambda^{\text{low}} \left[ \frac{\text{erg}}{\text{cm}^3 \text{ s}} \right] = \sum_i n_i n_{\text{H}} \xi_{\text{cpw}} \left[ L_{\text{e}}^{\text{low}}(X_i) f_{\text{ion}} + L_{\text{H}}^{\text{low}}(X_i) \right], \quad (40)$$

where summation is done over six elements: H, O, C, N, Si, and Fe, where applicable. Here,  $\xi_{\text{cpw}}$  is the cold plus warm gas fraction, and  $f_{\text{ion}} = n_e/n_{\text{H}}$  is the ionization fraction, the value of which for a given gas temperature  $T_{\text{g}}$  is taken from table 2 of Schure et al. (2009) for the collisionally ionized gas in thermal equilibrium for  $T_{\text{g}} > 10^{3.8}$  K. At lower temperatures,  $f_{\text{ion}}$  is set to a constant value of 0.01.

We note that most of the considered elements (C, Si, Fe, and O) have relatively low critical densities  $n_{\text{crit}}$  at which spontaneous and collisional de-excitations become comparable for some transition levels. Cooling due to these elements at  $n_{\text{H}} \gtrsim n_{\text{crit}}$  is proportional to  $n_i n_{\text{crit}}$  rather than to  $n_i n_{\text{H}}$ . We take this into account by multiplying Equation (40) with  $n_{\text{crit}}/(n_{\text{crit}} + n_{\text{H}})$  and taking  $n_{\text{crit}}$  from table 8 in Hollenbach & McKee (1989). We note that at a low numerical resolution the critical densities may never be reached.

### 3.2. High-temperature cooling

For the solar-metallicity plasma with temperature  $T \geq 10^4$  K, we have adopted the cooling rates of Böhringer & Hensler (1989), which include the line emission for most abundant elements and continuum emission due to free-free, two-photon, and recombination radiation. We have considered nine chemical elements (H, He, C, N, O, Ne, Mg, Si, and Fe), the total (line plus continuum) cooling efficiencies  $L^{\text{high}}(X_i)$  for which are plotted in Fig. 2 of Böhringer & Hensler (1989). These cooling efficiencies are normalized to  $n_e n_{\text{H}}$  and hence need to be multiplied by the ionization fraction  $f_{\text{ion}} = n_e/n_{\text{H}}$  to retrieve the values that can later be used in our hydro code. The total cooling rates in the high-temperature regime is then calculated as

$$\Lambda^{\text{high}} \left[ \frac{\text{erg}}{\text{cm}^3 \text{ s}} \right] = \sum_i L^{\text{high}}(X_i) f_{\text{ion}} (n_{\text{H}} \xi_{\text{cpw}})^2 \frac{n_i}{n_i^{\text{sol}}}, \quad (41)$$

where  $n_i$  is the current number density of element  $i$ ,  $n_i^{\text{sol}}$  is its number density at the solar abundance, and summation is performed over nine elements: H, He, C, N, O, Ne, Mg, Si, and Fe.

Figure 2 shows the cooling efficiency laid out in the following form

$$\sum_i \frac{n_i}{n_{\text{H}}} \left[ f_{\text{ion}} L_{\text{e}}^{\text{low}}(X_i) + L_{\text{H}}^{\text{low}}(X_i) \right] + f_{\text{ion}} L^{\text{high}}(X_i). \quad (42)$$

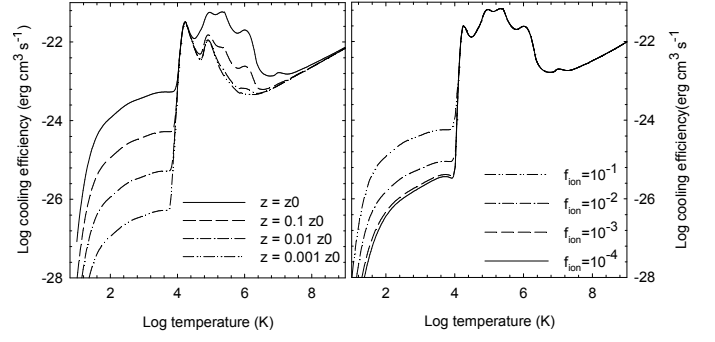


**Fig. 2.** Cooling efficiency of gas as a function of temperature for the ionization fraction  $f_{\text{ion}} = 1.0$  but varying metallicity (left panel) and for the gas with solar metallicity but varying ionization fractions  $f_{\text{ion}}$  (right column).

In particular, the left panel has  $f_{\text{ion}} = 1$  but varying metallicity and the right panel has the solar metallicity but varying  $f_{\text{ion}}$ . A strong dependence on the metallicity and ionization fraction for  $f_{\text{ion}} \gtrsim 10^{-3}$  is evident in the figure.

### 3.3. Gas temperature

In order to use the cooling rates described above, one needs to know the gas temperature  $T$ . The latter is calculated from the ideal equation of state  $P = \rho_{\text{g}} \mathcal{R} T_{\text{g}} / \mu$ , where  $\mathcal{R}$  is the universal gas constant, using the following expression for the mean molecular weight

$$\mu = \frac{\sum_i \rho_i + m_e f_{\text{ion}} n_{\text{H}}}{\sum_i n_i + f_{\text{ion}} n_{\text{H}}}, \quad (43)$$

where  $m_e$  is the electron mass and the summation is performed over all nine chemical elements considered in this study.

### 3.4. Avoiding the overcooling of SN ejecta

When the supernova energy is released in the form of the thermal energy, there may exist the risk of overestimating the gas cooling, which may lead to radiating away most of the released thermal energy. This occurs due to the fact that the cooling rate  $\Lambda$  is proportional to the square of gas number density, which, for a single-phase medium, may be significantly higher than what is expected in the case of a multi-phase medium for the hot supernova ejecta.

To avoid the spurious gas overcooling, we make use of the following procedure. We keep track of the hot SN ejecta by solving for the following equation for the hot gas density  $\rho_{\text{g,h}}$

$$\frac{\partial \rho_{\text{g,h}}}{\partial t} + \nabla \cdot (\rho_{\text{g,h}} \mathbf{v}_{\text{g}}) = \mathcal{S} - \frac{\rho_{\text{g,h}}}{\tau_{\text{c,h}}}, \quad (44)$$

The second term on the r.h.s. accounts for the phase transformation of the hot gas into the cold plus warm (CpW) component, where  $\tau_{\text{c,h}} = \epsilon / \Lambda_{\text{h}}$  denotes the cooling time of the hot component and the cooling rate  $\Lambda_{\text{h}}$  is calculated assuming the characteristic cooling efficiency of

$5 \times 10^{-23}$  ergs cm<sup>3</sup> s<sup>-1</sup> of the hot component with the typical temperature of  $10^8$  K (see Fig. 2 and Section 6)<sup>4</sup>.

Equation (44) is solved along with the system of equations (1)–(4) describing the evolution of the gas disk and the CpW gas fraction is calculated as  $\xi_{\text{cpw}} = (\rho_g - \rho_{g,h})/\rho_g$ . We then modify the cooling rates and the SFR by multiplying the total gas density  $\rho_g$  and the hydrogen number density  $n_H$  in Equations (40) and (41) and also in Equation (30) with  $\xi_{\text{cpw}}$  to retrieve the density of the CpW component. This procedure scales down the cooling rates and the SF rate according to the mass of the CpW component in each computational cell and helps to avoid overcooling and unphysically high SF rates.

### 3.5. Heating processes

#### 3.5.1. Cosmic ray heating

The cosmic ray heating efficiency is the product of the cosmic-ray ionization rate  $\xi_{\text{cr}}$  and the energy input per ionization  $\Delta Q_{\text{cr}}$ . We adopt  $\xi_{\text{cr}} = 4 \times 10^{-17}$  s<sup>-1</sup> based on the work of Van Dishoeck & Black (1986). The value of  $\Delta Q_{\text{cr}}$  is approximately 20 eV. The resulting heating rate due to ionization of hydrogen and helium atoms is

$$\Gamma_{\text{cr}} = 1.34 \times 10^{-27} G_0 (0.48 n_H + 0.5 n_{\text{He}}) \left[ \frac{\text{ergs}}{\text{cm}^3 \text{ s}} \right], \quad (45)$$

where the coefficients 0.48 and 0.5 are taken from table 6 in Hollenbach & McKee (1989). The quantity  $G_0$  represents the interstellar radiation field (IRF) normalized to the solar neighbourhood value, i.e. we make here the usual assumption that the cosmic ray intensity scales with the IRF. We calculate its value as  $G_0 = \text{SFR}_{\text{loc}}/\text{SFR}_{\text{MW}}$ , where  $\text{SFR}_{\text{loc}}$  is the local SFR in our models and  $\text{SFR}_{\text{MW}} = 1.0 M_{\odot} \text{ yr}^{-1}$  is the SFR in the Milky Way (Robitaille & Whitney, 2010).

#### 3.5.2. Photoelectric heating from small dust grains

The photoelectric emission from small grains induced by FUV photons can substantially contribute to the thermal balance of the interstellar medium at temperatures  $\lesssim 10^4$  K. We use the results of Bakes & Tielens (1994) and express the photoelectric heating rate per unit volume as

$$\Gamma_{\text{ph}} = 1.0 \times 10^{-24} \epsilon_{\text{ph}} G_0 n_H \xi_d \left[ \text{ergs cm}^{-3} \text{ s}^{-1} \right]. \quad (46)$$

The photoelectric heating efficiency  $\epsilon_{\text{ph}}$  is calculated from Figure 13 of Bakes & Tielens. We have also introduced the coefficient  $\xi_d = (M_d/M_{\text{HI}})/(M_d/M_{\text{HI}})_{\odot}$  to take into account a (possibly) different dust to gas mass ratio  $(M_d/M_{\text{HI}})$  in DGs. The latter is found using the following relation between the oxygen abundance (by number density) and the dust-to-gas mass ratio in dwarf galaxies (Lisenfeld & Ferrara, 1998)

$$12 + \log \left( \frac{\text{O}}{\text{H}} \right) = 0.52 C_d \log \left( \frac{M_d}{M_{\text{HI}}} \right), \quad (47)$$

where the normalization constant  $C_d = -5.0$  is derived from the corresponding quantities of the Small Magellanic Cloud. For the solar dust to gas mass ratio we adopt  $(M_d/M_{\text{HI}})_{\odot} = 0.02$ , typical for the interstellar medium in the Solar neighbourhood.

<sup>4</sup> In a more accurate approach,  $\Lambda_h$  can be directly calculated using equation (41)

## 4. Solution method

The equations of gas and stellar hydrodynamics are solved in cylindrical coordinates with the assumption of axial symmetry using a time-explicit (except for the gas internal energy update due to gas cooling/heating), operator-split approach similar in methodology to the ZEUS code (Stone & Norman, 1992). We use the same finite-difference scheme but, contrary to the ZEUS code, we advect the internal energy density  $\epsilon$  rather than the specific one  $\epsilon/\rho_g$  because the latter may give rise to undesired oscillations in some test problems (e.g. Clarke, 2010). Below, we briefly review the numerical scheme. The test results of our author's implementation of the code are provided in the Appendix.

The solution procedure consists of three main steps. Step 1: we update the gas and stellar components due to star formation and feedback. The corresponding ordinary differential equations describing the time evolution of  $\rho_g$ ,  $\rho_i$ ,  $\rho_g \mathbf{v}_g$ ,  $\epsilon$ ,  $\rho_s$ ,  $\rho_s \mathbf{v}_s$ , and  $\Pi_{ij}$  due to the source and sink terms involving  $\mathcal{D}$ ,  $\mathcal{D}^i$ ,  $\mathcal{S}$ ,  $\mathcal{S}^i$ , and  $\Gamma_*$  in equations (1)–(4) and (6)–(8) are solved using a first-order explicit finite-difference scheme. In Step 1, we also calculate the total gravitational potential of the gas and stellar components by solving for the Poisson equation (11) using the alternative direction implicit method described in Black & Bodenheimer (1975). The gravitational potential at the outer boundaries is calculated using a multipole expansion formula in spherical coordinates (Jackson, 1975). To save on computational time, we invoke the gravitational potential solver only when the relative change in the total (gas plus stellar) density exceeds  $10^{-5}$  (see Stone & Norman, 1992, for details).

Step 2: we solve for the gas hydrodynamics equations (1)–(4) excluding the source and sink terms that have been taken into account in the previous step. The solution is split into the transport and source substeps. During the former, advection is calculated using a third-order accurate piecewise-parabolic scheme of Colella & Woodward (1984) modified for cylindrical coordinates as described in Blondin & Lufkin (1993). During the latter, we update the gas momenta  $\rho_g \mathbf{v}_g$  due to gravitational and pressure forces and the gas internal energy  $\epsilon$  due to compressional heating using a solution procedure described in Stone & Norman (1992).

At the end of Step 2, a fully implicit backward Euler scheme combined with Newton-Raphson iterations is used to advance  $\epsilon$  in time due to volume cooling  $\Lambda$  and heating  $\Gamma$  rates. In order to monitor accuracy, the total change in  $\epsilon$  in one time step is kept below 10%. If this condition is not met, we employ local subcycling in a particular cell by reducing the time step in the backward Euler scheme by a factor of two (as compared to the global hydrodynamics time step) and making two individual substeps in the cell where accuracy was violated. The local time step may be further divided by a factor of two until the desired accuracy is reached. The local subcycling help to greatly accelerate the numerical simulations as one need not to repeat the solution procedure for every grid cell.

In Step 2, we also add tensor artificial viscosity to equations (3) and (4) to smooth out strong shocks as described in Stone & Norman (1992). As pointed out in Tasker et al. (2008) and discussed in Clarke (2010), the ZEUS code with the von Neumann & Richtmyer (1950) definition of the artificial viscosity performs poorly on multidimensional tests such as the Sedov point explosion, yielding non-spherical so-



lutions that may overshoot or undershoot the analytic one. We demonstrate in Section A.2 that using the tensor artificial viscosity and the proper choice of the artificial viscosity parameter  $C_2 = 6$  can greatly improve the code performance. However, contrary to the Stone & Norman suggestion to discard the off-diagonal terms of the viscous stress tensor, we demonstrate that in fact these terms should be retained and the most general formulation of the artificial viscosity stress tensor should be used

$$\mathbf{Q} = \begin{cases} l^2 \rho_g \nabla \cdot \mathbf{v}_g [\nabla \mathbf{v}_g - \mathbf{e}(\nabla \cdot \mathbf{v}_g)/3] & \text{if } \nabla \cdot \mathbf{v}_g < 0 \\ 0 & \text{if } \nabla \cdot \mathbf{v}_g \geq 0 \end{cases}, \quad (48)$$

where  $\mathbf{e}$  is the unit tensor,  $l = C_2 \max(dx)$ , and  $dx$  is the grid resolution in each coordinate direction. For the reasons of the code stability, all components of the viscous stress tensor  $\mathbf{Q}$  should be defined at the same position on the grid, i.e., at the zone centers (contrary to the ZEUS code which defines the off diagonal components of rank-two tensors at the zone corners). The Courant limitations on artificial viscosity may be substantial in regions with strong shocks. Therefore, we apply local subcycling (in the same manner as it is done with the internal energy update due to heating/cooling) when the local viscous time step becomes a small fraction of the global hydrodynamics time step.

In step 3, we solve for the stellar hydrodynamics equations (6)–(8) excluding the source and sink terms that have been taken into account during step 1. The solution procedure is similar to that for the gas hydrodynamics equations, since both systems are defined essentially on the same grid stencil—a powerful advantage of the stellar hydrodynamics approach. All components of the velocity dispersion tensor are defined at the cell centers to be consistent with the definition of the stellar artificial viscosity tensor  $\mathbf{Q}$ . The latter is defined by analogy to its gas counterpart with the gas density and velocity in equation (48) substituted with the stellar density and velocity. Additional terms  $-\nabla \cdot \mathbf{Q}$  and  $-Q_{ik} : (\nabla \mathbf{v}_s)_{kj} - Q_{jk} : (\nabla \mathbf{v}_s)_{ki}$  have been added to the r.h.s. of equations (7) and (8), respectively, to take into account the viscous stress and heating due to artificial viscosity.

Finally, the global time step for the next loop of simulations is calculated using the Courant condition modified to take into account star formation and feedback. In particular, two time step delimiters of the form

$$\Delta t_{s.f.} < \frac{C_3 \rho_g}{\mathcal{D}}, \quad (\text{star formation}), \quad (49)$$

$$\Delta t_{f.b.} < \frac{C_3 \rho_s}{\mathcal{S}}, \quad (\text{stellar feedback}) \quad (50)$$

are added to the usual Courant condition to avoid obtaining negative values of the flow variables. The safety coefficient  $C_3$  is set to 0.5. Some modification to the classic Courant condition is required for the stellar hydrodynamics part because the stellar velocity dispersion tensor  $\mathbf{\Pi}$  is anisotropic in general. To calculate the stellar hydrodynamics time step, we use the following form

$$\Delta t_{st} = \min \left[ \frac{dx}{|\mathbf{v}_s| + \max \bar{\Pi}_{ii}} \right], \quad (51)$$

where  $\max \bar{\Pi}_{ii}$  is the maximum diagonal element of the diagonalized velocity dispersion tensor and minimum is taken over all grid zones.

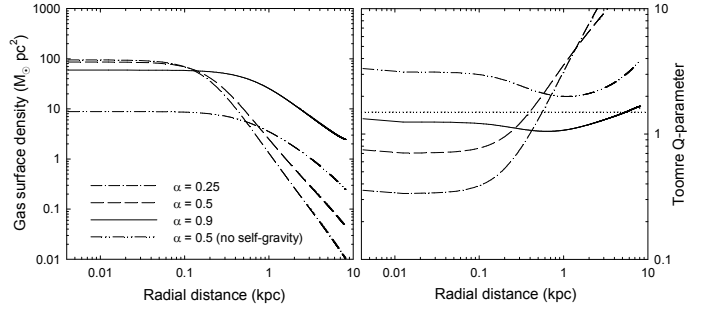


**Fig. 3.** Initial radial profiles of the gas surface density  $\Sigma_g$  (right) and Toomre  $Q$ -parameters (left) in models with different rotational support against gravity as indicated by the  $\alpha$ -parameter. The horizontal dotted lines define the critical values of  $Q$ -parameter below which star formation is supposed to occur (see the text for more details).

## 5. The chemo-dynamical evolution of model dwarf galaxies

Our numerical code has been extensively tested using a standard set of test problems as described in the Appendix. However, even a perfect performance on the standardized tests does not guarantee meaningful results on real problems when all parts are invoked altogether.

Therefore, in this section, we consider the evolution of several representative models of DGs in order to test the overall code performance and to demonstrate the simulation methodology and recipes described in the previous sections. In particular, we wish to emphasize the effect of stellar dynamics and initial conditions on the simulation outcomes. Moreover, we will show the results of simulations with different degrees of rotational support against gravity parameterized by the  $\alpha$ -parameter defined as  $\alpha = v_\phi/v_{\text{circ}}$ , where  $v_\phi$  and  $v_{\text{circ}}$  are the rotation and circular velocities, the latter being the maximum velocity calculated from the assumption that all support against gravity comes from rotation (i.e., zero gas pressure gradients). We consider three different degrees of rotational support:  $\alpha = 0.25, 0.5, 0.9$ . The resulting initial geometries vary from flat-like for large values of  $\alpha$  to roundish for small  $\alpha$ .

Our initial configuration consists of a self-gravitating gaseous disk submerged into a fixed DM halo described by a cored isothermal sphere (e.g. Silich & Tenorio-Tagle, 2001). We focus on models with a DM halo mass of  $10^9 M_\odot$  and initial gas temperatures of  $10^4$  K. We apply the solution procedure described in Vorobyov et al. (2012) to construct self-gravitating equilibrium configurations for different values of  $\alpha$ . The initial gas metallicity  $Z_g$  is set to  $10^{-2} Z_\odot$ , the ratio of specific heats  $\gamma$  to  $5/3$ , and the redshift is set to zero. The number of grid zones is 1000 in each coordinate direction, resulting in the effective numerical resolution of 8 pc everywhere throughout the computational domain. We impose the equatorial symmetry at the midplane and the reflection boundary condition at the axis of symmetry. At the other boundaries, a free outflow condition is applied.

Figure 3 presents the initial gas surface density  $\Sigma_g$  (left panel) and the Toomre  $Q$ -parameter (right panel) as a function of the midplane distance in the  $\alpha = 0.25$  model 1 (dash-dotted lines),  $\alpha = 0.5$  model 2 (dashed lines), and  $\alpha = 0.9$  model 3 (solid lines). Evidently, the  $\alpha = 0.25$  model is characterized by the most centrally condensed gas distribution.

**Table 1.** Model parameters

Model	$\alpha$	$M_g(\leq 1 \text{ kpc})$ $M_\odot$	$M_g(\leq 3 \text{ kpc})$ $M_\odot$	$M_g(\text{total})$ $M_\odot$	self-consistent initial model	stellar motion
1	0.25	$2.1 \times 10^7$	$2.9 \times 10^7$	$3.5 \times 10^7$	yes	yes
2	0.5	$2.8 \times 10^7$	$4.5 \times 10^7$	$6.4 \times 10^7$	yes	yes
3	0.9	$1.1 \times 10^8$	$4.1 \times 10^8$	$1.0 \times 10^9$	yes	yes
4	0.5	$2.8 \times 10^7$	$4.5 \times 10^7$	$6.4 \times 10^7$	yes	no
5	0.5	$1.0 \times 10^7$	$4.5 \times 10^7$	$1.2 \times 10^8$	no	yes

The horizontal dotted line marks a critical  $Q$ -parameter of 1.5 below which star formation is supposed to occur according to the stability analysis of self-gravitating disks by Toomre (1964) and Polyachenko et al. (1997)<sup>5</sup>. Evidently, the  $\alpha = 0.25$  and  $\alpha = 0.5$  models are strongly inclined to star formation in the inner 0.5 kpc, while outside this radius the conditions are not favourable due to a rather steep drop in the gas surface density with distance. On the other hand, the  $\alpha = 0.9$  model is characterized by a much shallower profile of  $\Sigma_g$ , resulting in a significantly larger galactic volume prone to star formation. The parameters of our models are listed in Table 1, where  $M_g(r \leq 1 \text{ kpc})$ ,  $M_g(r \leq 3 \text{ kpc})$ , and  $M_g(\text{total})$  are the gas masses inside a spherical radius of 1 kpc, 3 kpc and the total gas mass in the computational domain of  $8.0 \times 8.0 \text{ kpc}^2$ .

Evidently, the gas mass increases with increasing  $\alpha$ , which is explained by the fact that models with higher rotation can support a higher gas mass against gravity of the DM halo. We note that the maximum gas mass is also limited by the action of gas self-gravity (Vorobyov et al., 2012). As the  $\alpha = 0.5$  model demonstrates, switching off the gas self-gravity leads to a factor of two increase in the total gas mass.

When constructing the initial gas density distribution in models 1, 2, and 3, we have chosen the same “seed” value for gas number density in the galactic center equal to  $10 \text{ cm}^{-3}$ . This was done in order to make the initial volume densities and temperatures in the galactic center similar in each model. We could have decreased the seed value in models 2 and 3, trying to adjust the total mass in these models to that obtained in model 1, but then the initial conditions for star formation would also have changed. In addition, it was not clear which mass to take as the reference value, because different values are obtained when integrating over different radii due to variations in the radial density profiles.

### 5.1. The role of $\alpha$

In Figure 4 we show a comparison of the gas volume density ( $\rho_g$ ) distribution in three model galaxies differing for the value of  $\alpha$ . Four representative time snapshots are taken for each model. The  $\alpha=0.9$  model 3 is characterized by the largest degree of flattening, due to the large centrifugal forces. A notable flaring in the initial gas density distribution of model 3 can be seen in the upper-right panel. This means that the vertical distribution at  $R = 0$  is characterized by a very steep density and pressure gradient. The over-pressurized superbubble created by the stellar feedback preferentially expands along this direction and a bipolar outflow is soon created. The external parts of the

<sup>5</sup> For a more detailed analysis of these star formation criteria see Vorobyov et al. (2012).

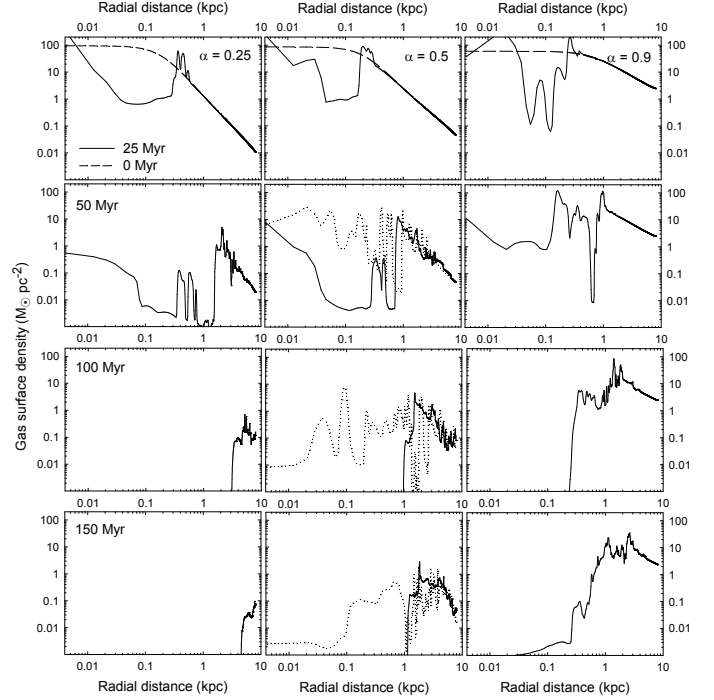


**Fig. 5.** Gas surface density as a function of radius for the same models and at the same moments in time as in Figure 4. In the upper panels the initial density distribution is also indicated (dashed lines). The dotted lines in the middle column also show the distribution for the  $\alpha = 0.5$  model without stellar motion (see Section 5.2).

disk are not affected by the bipolar outflow and even after  $t = 150 \text{ Myr}$  the gas density of the disk at radii larger than 1 kpc is quite large. Some of the material in the bipolar outflows falls back onto the disk. As a result, the fraction of pristine gas lost by this model is relatively small, in spite of the fact that the galactic outflow is very prominent and affects a large fraction of the computational domain. However, the freshly produced metals can be easily channelled out of the galaxy.

At the other extreme is the  $\alpha=0.25$  model 1. Here, the initial gas density configuration is almost spherical and the pressure gradient is only slightly steeper in the vertical direction than in the horizontal one. A bipolar outflow soon develops but there is significant gas transport also along the disk and, after 100 Myr, all the gas in the central part of the galaxy (up to a radius of almost 5 kpc) has been completely blown away.

This effect is illustrated in Figure 5, where the gas surface density as a function of radius is plotted for our three reference models at the same moments in time as in Figure 4. After 100 Myr there is almost no gas left in

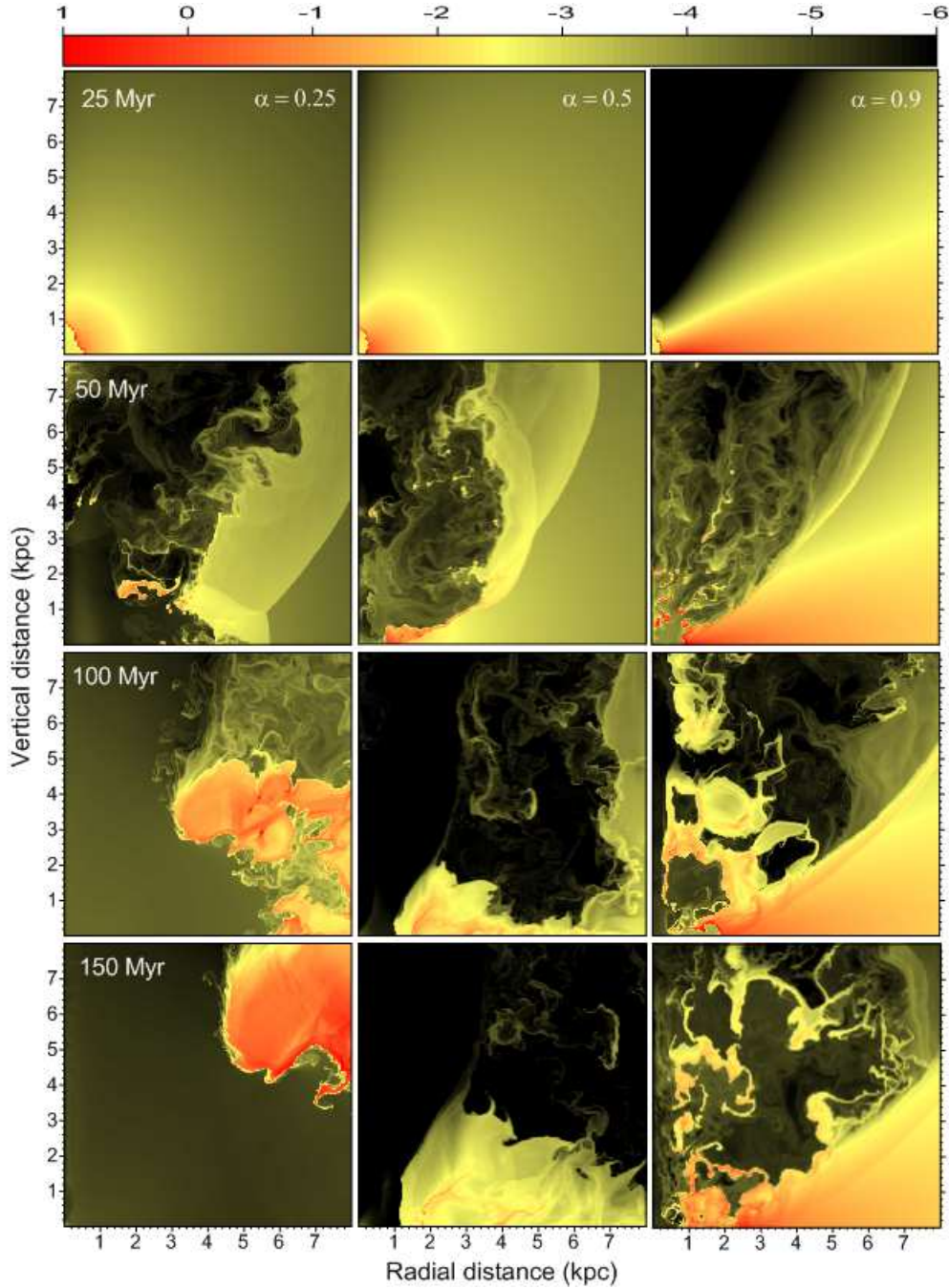


**Fig. 4.** Gas density distribution of three model galaxies differing for the amount of rotational support: the  $\alpha=0.25$  model 1 (left column), the  $\alpha=0.5$  model 2 (middle column), and the  $\alpha=0.9$  model 3 (right column). The time passed from the beginning of numerical simulations is indicated in the leftmost image of each row. The density scale (in  $\text{cm}^{-3}$ ) is shown in the upper strip.

the inner 3 kpc in the  $\alpha=0.25$  model 1, whereas a central hole in the  $\alpha=0.9$  model 3 is of a much smaller radius, hardly exceeding 0.2 kpc, and the gas distribution at  $R > 2$  kpc is nearly undisturbed. This different galactic evolution, depending on the initial distribution of gas, has been already described in the literature (see in particular Recchi & Hensler, 2013), but here we show it in a more realistic context of self-gravitating initial gas configurations.

A direct way to appreciate the role of  $\alpha$  on the evolution of our model galaxies is by calculating the ejected gas mass for various models. Figure 6 presents the fraction of ejected

gas mass vs. time in models 1–3. We find this value by calculating the amount of gas that leaves the computational domain ( $8 \times 8 \text{ kpc}^2$ ) with velocities greater than the escape velocity at the computational boundary. The fraction of ejected mass is very large in the  $\alpha=0.25$  model, because of the blow-away described above, but it is very small for the  $\alpha=0.9$  model because only a small fraction of the gas originally present in the disk is involved in the galactic outflow. The dash-double dotted line presents the fraction of ejected mass in the  $\alpha = 0.5$  model 2, in which the motion of star was artificially suppressed (see Sect. 5.2 for details.)



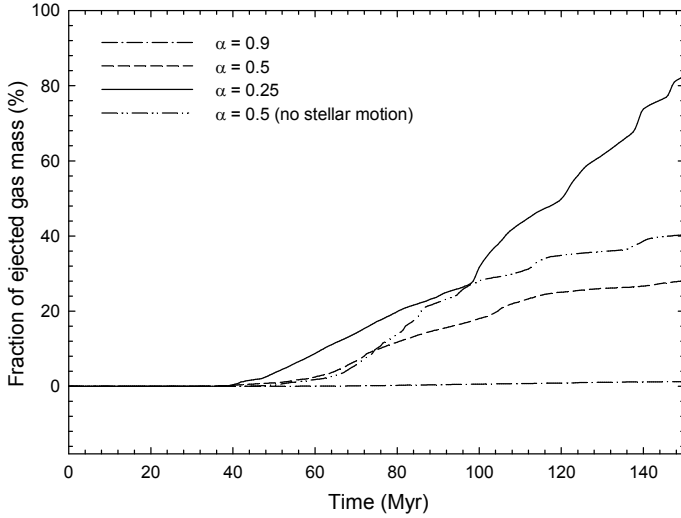


**Fig. 6.** Fraction of ejected gas mass as a function of time for the models with different values of  $\alpha$ . The dashed-double dotted line refers to a model in which the stellar motion has been artificially suppressed (see Sect. 5.2).

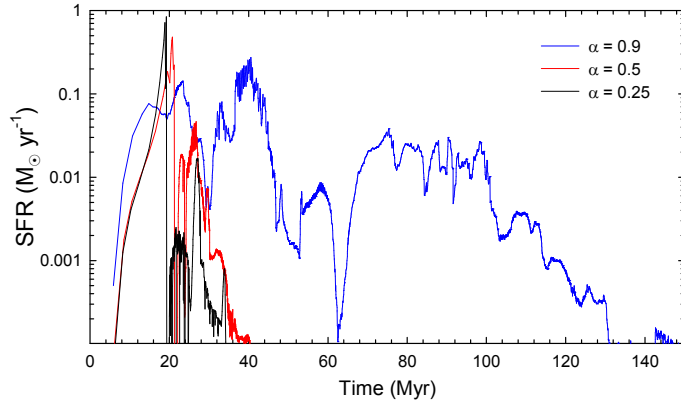


**Fig. 7.** Star formation rates vs. time in three models differing in the value of the centrifugal support  $\alpha$ .

The different gas dynamics of the three reference models shown in Figure 4 has dramatic consequences also for the star formation histories. Figure 7 presents the star formation rate vs. time. Evidently, the strong star formation feedback in the  $\alpha=0.25$  model shuts off star formation after  $\sim 30$  Myr. The  $\alpha=0.5$  model behaves similarly, although star formation is shut off slightly later. On the other hand, the  $\alpha=0.9$  model is able to sustain star formation for a longer time, mainly because the disk still remains gas-rich and the conditions for the star formation to occur are fulfilled in many grid cells.

Figure 8 presents the distribution of the stellar volume density  $\rho_s$  as a function of time and for the same models and at the same time instances as in Figure 4. In addition, the right-hand column presents the volume density of high-mass stars  $\rho_s^h$ . We can clearly see that the stellar distribution in the  $\alpha = 0.25$  model is more homogeneous and isotropic than in the  $\alpha = 0.9$  model, wherein many stars tend to be located along the polar axis. We note, however, that owing to a preferable concentration of gas toward the midplane in the  $\alpha=0.9$  model, a significant fraction of stars is also distributed near the midplane, constituting a stel-

lar disk. This effect is much less evident for the models with  $\alpha=0.5$  and  $\alpha=0.25$ . To quantify this, we calculated the fraction of the total stellar mass confined within a vertical height of 1 kpc and 2 kpc. It turns out that in the  $\alpha = 0.25$  model these values are 37% and 62%, respectively, whereas in the  $\alpha = 0.9$  model they are 90% and 94%, indicating a much more compact stellar distribution in the higher- $\alpha$  model. Finally, a comparison of the distribution between  $\rho_s$  (the total stellar density) and  $\rho_s^h$  in the  $\alpha=0.9$  model indicates that stars are preferentially forming at low galactic altitudes  $\lesssim 1$  kpc, but are later spread out owing to their own initial dispersion ( $5 \text{ km s}^{-1}$ ) and, especially, owing to significant bulk velocities inherited from parental gas clouds. The off-plane star formation is taking place predominantly in dense gaseous clumps and on the cavity walls.

## 5.2. The role of the stellar motion and the initial gas distribution

In this work, we employ the moments of the collisional Boltzmann equation to describe the motion of stars. In addition, we start our simulations from self-consistent initial equilibrium conditions that were built taking gas self-gravity into account (in some studies, the initial configuration is constructed without taking gas self-gravity into account, although during the dynamical evolution the gas self-gravity may be included). It is instructive to study how these two new recipes affect the dynamics of our model galaxies.

In Figure 9 we show the gas volume density in three models with  $\alpha=0.5$  at four representative evolution times. In particular, the left-hand-side column shows the evolution of our reference model 2, already shown in Figure 4. The middle column shows model 4, in which the stellar dynamics has been artificially suppressed. Stars are allowed to form, but they are effectively motionless and are fixed to their birthplaces until they die. Evidently, the final gas distribution in model 4 is clumpy: the galactic volume is filled with moving cometary-like clouds. The increase in the number of clumps is caused by a reduced feedback in the absence of stellar motion. The moving clumps leave behind the newly-born stars so that part of the stellar energy is released outside the clumps, which makes it easier for the clumps to survive. In the presence of stellar motion, the newly-born stars follow the gas clumps (at least for some time) due to the fact that they inherit the gas velocity at the formation epoch, releasing the stellar energy inside the clumps and dispersing most of them.

The final gas distribution in model 2 is smooth and shows no cometary-like structures. At the same time, the outflow in model 4 clears a larger hole near the midplane than in the reference model. The combination of these two effects results in a rather chaotic gas surface density distribution shown in the middle panel of Figure 5 by the dotted lines. We also note that model 4 is characterized by a somewhat higher star formation feedback, as is indicated by the fraction of ejected gas mass shown by the dot-dot-dashed line in Figure 6.

The increased feedback in the model without stellar motions is likely due to the fact that the energy of both supernova explosions and stellar winds is released in regions characterized by a systematically higher temperature and lower density than in the reference model. This is because



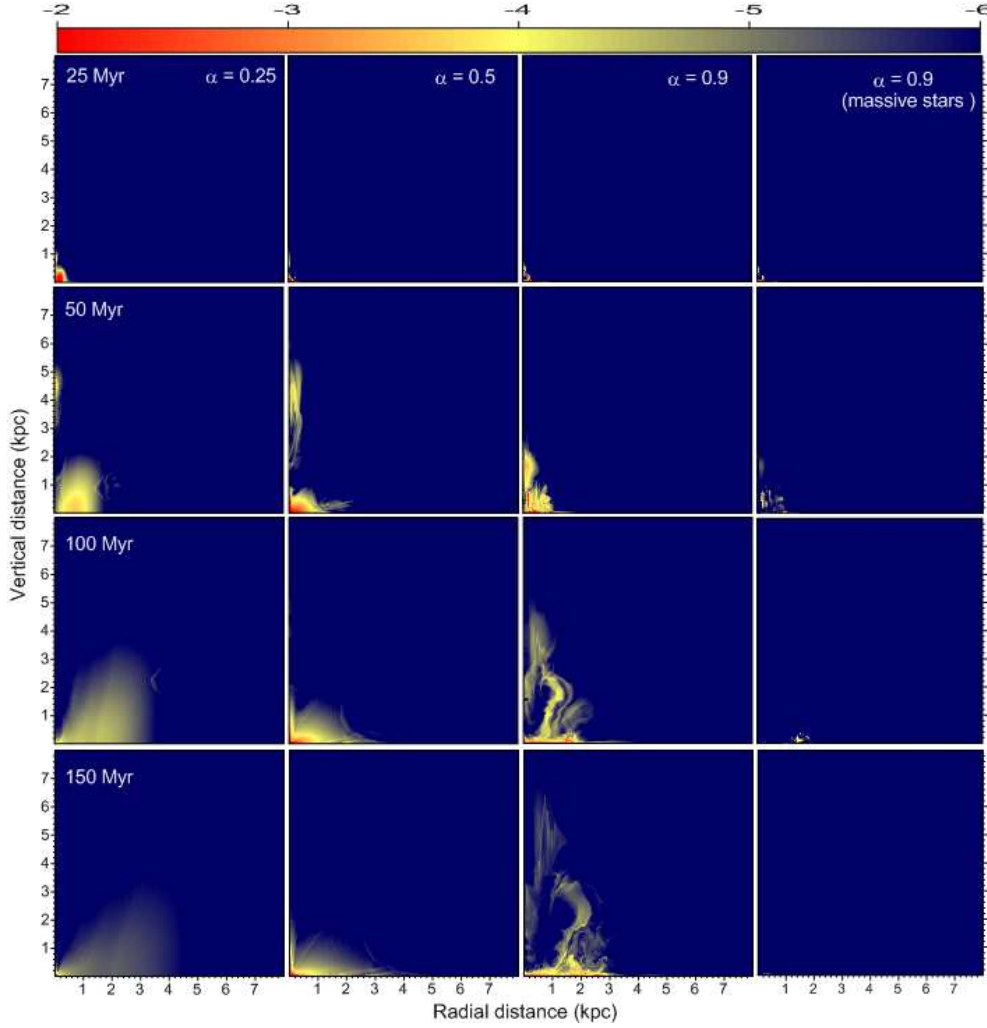


**Fig. 8.** Similar to Fig. 4, but now for the stellar volume density distribution. The scale bar is in  $M_{\odot} \text{ pc}^{-3}$ . The right-hand column presents only the massive stars.

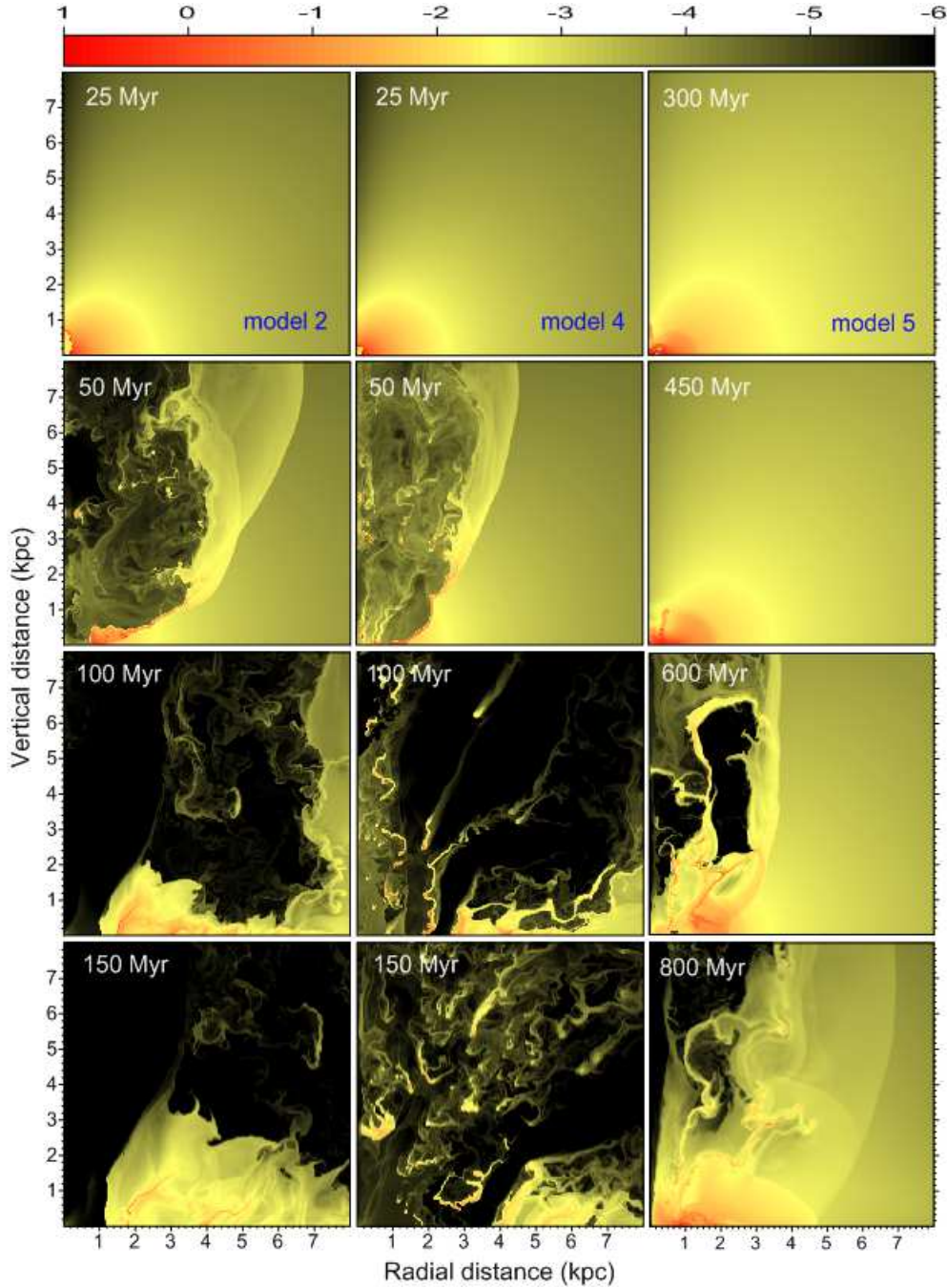
star formation creates regions of slightly lower density compared to the surrounding gas, and stellar winds stir and heat up the circumstellar gas. If stars are motionless, then their feedback is confined to their birthplaces. On the other hand, if stellar motion is allowed, stars can move to neighboring regions, where the density is likely to be higher and where stellar winds have not yet heated the gas. The feedback will be thus less effective. This conclusion is at variance with that of Slyz (2007), who showed that stellar motion makes the feedback more effective and can even solve the overcooling problem. This different outcome is probably due to the lack of feedback from stellar winds in Slyz’s models.

Figure 10 presents the stellar volume density distributions for the same models as in Figure 9. The left-hand column corresponds to the reference model 2, already shown in Figure 8, while the middle column presents model 4, in which stellar motions are suppressed. Evidently, models with and without stellar motion produce strikingly different stellar distributions. The stellar distribution in the reference model is rather smooth, whereas in the model without stellar motions most of the stellar content is confined to the midplane and in the inner region. In fact, the fraction of the total stellar mass confined within a vertical height of

0.3 kpc (from the midplane) is 82% for the reference model, but this value increases to 98% for the model without stellar motions. The curious stellar stripes visible in the middle column are caused by the development of a gaseous supershell: many stars tend to form on the walls of this supershell and, as a consequence, their position reflects the shell’s expansion. The lack of stellar motion makes these structures permanent. The fact that these structures are not observed in real galaxies outlines the importance of a proper treatment of stellar dynamics in numerical simulations of DGs.

Finally, we investigate the question of how the choice of the initial gas density distribution can influence the subsequent evolution of dwarf galaxies. For this purpose, we choose  $\alpha = 0.5$  and construct two initial gas density distributions: one with the gas self-gravity taken into account and the other without it. To make the comparison between models with and without self-gravity easier, we require that the gas mass within the 3-kpc radius be similar in both models. The model with the initial equilibrium distribution taking gas self-gravity into account is in fact our model 2 considered above, while its counterpart is further referred as model 5 (see Table 1 for model parameters).

The initial radial profiles of the gas surface density and the Toomre  $Q$ -parameter in model 5 are shown in Figure 3



**Fig. 9.** Time evolution of the gas volume density in three models with  $\alpha=0.5$ . The l.h.s. column presents the time evolution in model 2, already shown in Fig. 4. The middle column shows model 4, in which the motions of stars are artificially suppressed. In the r.h.s. column we show model 5, for which the initial equilibrium distribution was constructed without taking gas self-gravity into account. Note the different evolutionary times in the latter model.

by the dash-dot-dotted lines. Not surprisingly, the initial gas distribution in model 2 is more centrally condensed than in model 5: gas self-gravity creates an additional gravity pull towards the galactic center<sup>6</sup>, resulting in a denser initial configuration. For instance, the total gas mass in the inner sphere of 1 kpc in the initial model without self-gravity is  $\approx 10^7 M_\odot$ , while this value rises by a factor of 2.8 in the model with self-gravity. As a consequence, the Toomre  $Q$ -

parameter is initially greater than 2.0 everywhere and star formation is effectively suppressed.

The right-hand column in Figure 9 presents the gas volume density distribution in model 5. We emphasize that the gas self-gravity in this model is neglected only when building the initial distribution; in the subsequent evolution the gas self-gravity is however turned on again. Evidently, the evolution of model 5 is notably slower owing to the fact that star formation is initially suppressed. The gas cools and contracts and only after 120 Myr the conditions for star formation become favourable in the galactic center, whereas

<sup>6</sup> The total gas and DM masses are comparable in the inner several kpc.

a vigorous star formation feedback is seen in model 2 already after 50 Myr of the evolution. The initial slow start in model 5 is consistent with a long dynamical timescale in this model. For the mean gas volume density in the inner 1 kpc of  $4 \times 10^{-25} \text{ g cm}^{-3}$ , the corresponding free-fall time in model 5 is approximately 110 Myr, which is consistent with the time epoch of the first star formation episode in this model. Due to significant thermal support and radially increasing dynamical timescale (density drops with radius), it takes several dynamical timescales to adjust to a state similar to that of model 2. By the end of simulations in model 5 (800 Myr), the outflow is still not as strong as in its counterpart model 2 and the central gap has not yet developed.

The right-hand column in Figure 10 presents the stellar volume density distribution in model 5. A visual inspection of the l.h.s. and r.h.s. models reveals that the stellar distributions in models 2 and 5 are in general similar (but note the difference in ages 150 vs. 800 Myr), though the stars in the latter model are distributed somewhat more irregularly. By the end of numerical simulations, the total mass of formed stars in the 800-Myr-old model 5 is still a factor of 4 lower than in the 150 Myr-old model 2, highlighting a much slower evolution in the model that starts from a non-self-consistent initial configuration, i.e. without initial gas self-gravity.

## 6. Discussion and model caveats

In this work, we did not aim at a detailed comparison of our numerical simulations with observed DGs, which is our task for subsequent studies. Instead, we have chosen three typical models for DGs with different rotational support against gravity to test the code performance on global simulations, and not just on a predefined set of classic test problems. The current version of the code assumes axial symmetry and neglected chemical reactions, which leaves us a wide door for future improvements. At the same time, we have managed to develop an efficient mathematical recipe for describing the phase transition from stars into gas using the continuity equation for the mean stellar age (see Section 2.6).

As already mentioned in the text, some simulation parameters have been chosen without a detailed parameter study or without an in-depth analysis. We avoid such a detailed study for the sake of clarity and in order to make the paper more concise and readable. A deeper parameter study will be performed in follow-up papers. It is nevertheless important to point out the potential caveats in the choice of some parameters.

- $\epsilon_{\text{sw}}$  (see Sect. 2.7.3.): Massive and intermediate-mass stars expel a significant fraction of their mass by stellar winds. Although their lifetimes shorten with mass, the mass-loss rates increase disproportionately, so that for solar abundances the total wind energy of most massive stars exceeds that of SNeII over the stellar lifetime. For radiation-driven HII regions, Lasker (1967) stated that the ISM is heated only by a very low amount and derived analytically an efficiency of 1%, because the ionizing radiation energy is almost instantaneously lost by line emission and only the expansion of HII regions steers up the surrounding ISM. Although the additional wind power amounts to almost 10% of the radiation energy, it is expected to deposit a larger frac-

tion as the thermal and kinetic ISM energies. Since in most chemo-dynamical simulations (Theis et al., 1992; Samland et al., 1997) the Ly continuum radiation is applied with an efficiency of  $10^{-3}$ ,  $\epsilon_{\text{sw}}$  is assumed to 100%. This value is also used here.

- $\epsilon_{\text{SN}}$  (see Sect. 2.7.1.): For the thermalization efficiency of the SNII explosion, i.e. the fraction of the explosion energy transferred to gas thermal energy we have adopted the value  $\epsilon_{\text{SN}} = 1.0$  for simplicity and in order to avoid further parameter studies. The thermalization efficiency has been subject to considerable studies in the past. Thornton et al. (1998) performed single 1D supernova explosion models and derived  $\epsilon_{\text{SN}} = 0.1$ . Estimates from cumulative SNII explosions, forming superbubbles, suggest a significant dependence of  $\epsilon_{\text{SN}}$  on the temperature and density of the external medium (Recchi et al., 2001; Recchi, 2014). A different approach, where the contribution of a whole stellar population is considered (Melioli & de Gouveia Dal Pino, 2004) clearly shows that  $\epsilon_{\text{SN}}$  is a function of time. We have performed a test simulation adopting  $\epsilon_{\text{SN}} = 0.1$ . The extent of the galactic winds was reduced in this case, but not by a large factor. It is in fact important to remark that with our formulation for the SFR (see Eq. 30), a great deal of self-regulation is achieved. In fact, the larger  $\epsilon_{\text{SN}}$ , the larger the heating of the surrounding medium, the higher the probability that the star formation is quenched for a period of time (see Koeppen et al., 1995, for more details on self-regulated star formation). Thus, although we plan to make more careful choices of  $\epsilon_{\text{SN}}$  in follow-up papers, this parameter appears not to change drastically the results of the simulations.
- $n_{\text{cr}}$  (see Sect. 2.7.4). The threshold density above which star formation is allowed,  $n_{\text{cr}} = 1 \text{ cm}^{-3}$  has been chosen in compliance with other numerical studies (Springel & Hernquist, 2003; Recchi et al., 2007). Also in this case, many different values for  $n_{\text{cr}}$  have been chosen in the literature and detailed studies on the effect of this parameters have been performed. In the framework of  $\Lambda$ CDM cosmological simulations,  $n_{\text{cr}}$  of  $0.1 \text{ cm}^{-3}$  is generally used (Katz, 1992) and its effect on the star formation was studied, e.g., by Kay et al. (2002), but also applied to much larger resolutions of smooth-particle hydrodynamics applications (Stinson et al., 2006). It appears that an extremely large value of (up to  $100 \text{ cm}^{-3}$  Governato et al., 2010) is required to obtain DGs with structural properties similar to the observed ones (but see also Pilkington et al., 2011). Quite generally, the star formation density threshold should be set based on the density at which gravitational instabilities can be resolved (see e.g. Truelove et al., 1997). This leads for instance Stinson et al. (2013) to assume a threshold of  $9.3 \text{ cm}^{-3}$  based on their adopted resolution. Clearly, our choice of  $n_{\text{cr}}$  is simplistic and deeper studies are required in follow-up publications. We notice only that in our simulation only a tiny fraction of gas reaches densities larger than a few tens of  $\text{cm}^{-3}$ , therefore the adoption of very large values of  $n_{\text{cr}}$  would lead to extremely localized and sporadic star formation. We notice also that the very large feedback achieved in the simulations of Governato et al. (2010) is certainly able to produce modelled DGs with structural properties similar to the observed ones, but it is not clear whether the chemical properties can be equally well reproduced. A very large

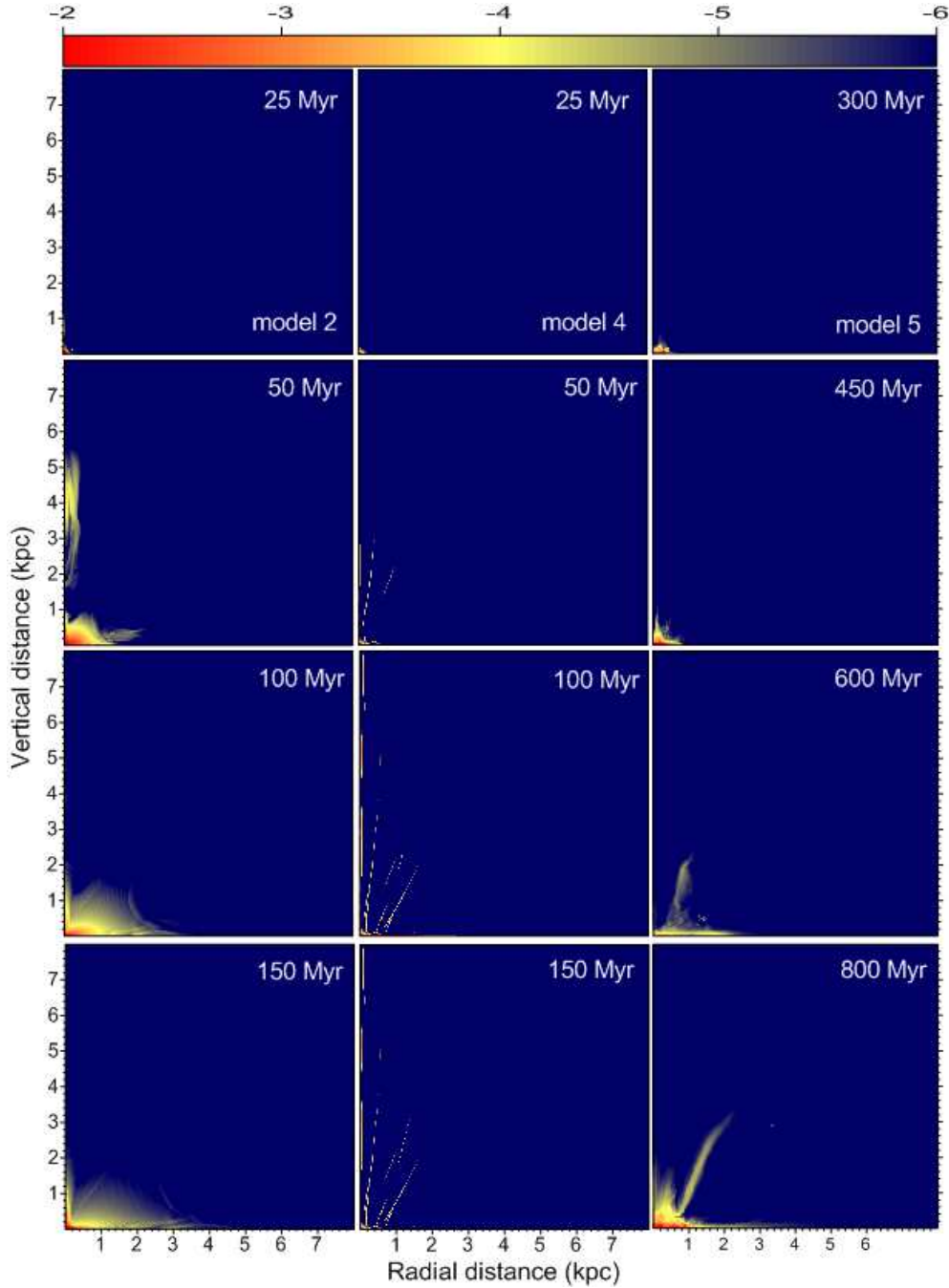


**Fig. 10.** Similar to Figure 9, but now for the stellar volume density distribution.

feedback can create galactic winds, able to expel the large majority of metals, freshly produced in the galaxy, thus at the end of the evolution the model galaxy should be almost deprived of heavy elements.

- $\Lambda_h$  (see Sect. 3.4). The cooling function typical of hot gas  $\Lambda_h$ , which has been used to calculate the cooling timescale of the hot SN ejecta, has been estimated based on a temperature of the hot ejecta of  $10^8$  K. It must be admitted that this temperature only holds just after the SN explosion, but the ejecta cools significantly afterwards. Nevertheless, the thermal SN energy has been varied artificially to probe its influence on galactic winds (Dalla Vecchia & Schaye, 2012). We note, however, that we are in the cooling regime dominated by

bremsstrahlung, and the temperature dependence of the cooling function is not so severe (the cooling is approximately proportional to  $\sqrt{T}$  in this temperature range).

## 7. Conclusions

In this paper, we presented the stellar hydrodynamics approach for modeling the evolution of DGs, paying special attention to the co-evolution of gas and stars. The distinctive feature of our models is how we treat the stellar component. Unlike many previous studies that use various versions of the N-body method to compute the dynamics of stars, we employ the stellar hydrodynamics approach based on the moments of the collisionless Boltzmann equa-



tion, originally introduced by Burkert & Hensler (1988), and applied and further developed by Theis et al. (1992); Samland et al. (1997); Vorobyov & Theis (2006, 2008); Mitchell et al. (2013); Kulikov (2014). For the first time, we provided an effective mathematical recipe for describing the death of stars in the framework of stellar hydrodynamics using the concept of a mean stellar age. We performed an extensive testing of our numerical scheme using classical and newly developed test problems, paying particular attention to the proper recipe for artificial viscosity in order to achieve the best agreement with the analytical solution for the Sedov test problem.

We demonstrate the success of our numerical approach by simulating the evolution of three DGs differing in the amount of rotation described by the spin parameter  $\alpha=0.25$ ,  $\alpha=0.5$ , and  $\alpha=0.9$ . In agreement with previous studies, models with low values of  $\alpha$  are characterized by stronger outflows, ejecting a larger amount of gas from the galaxy. This is due to the fact that the initial gas distribution in the low- $\alpha$  models is almost spherical, so that the gas pushed by the stellar feedback expands almost isotropically. On the contrary, models with high values of  $\alpha$  exhibit a disk-like initial gas distribution with a pronounced radial flaring. The pressure gradient in the vertical direction in these models is very steep, which favours the development of bipolar galactic outflows. The transport of gas in the horizontal direction (i.e. along the galactic midplane) is very limited, and therefore this model is able to keep most of the initial gas bound to the galaxy. The fraction of ejected gas (i.e., the fraction of gas that leaves the computational domain with a speed higher than the escape speed) is only a few percent for the  $\alpha = 0.9$  model, but it raises to 80% for the model with  $\alpha = 0.25$ .

At the same time, models with a low value of  $\alpha$  produce a more diffuse stellar population than models with higher  $\alpha$ . Only models with  $\alpha \geq 0.5$  reveal the formation of a definite stellar disk component. We demonstrate the importance of the stellar dynamics by artificially turning off stellar motions. In this case, the resulting stellar population is mostly concentrated to the midplane and shows stripe-like structures emanating from the galactic center, which are not observed in real galaxies.

Stars start heating the natal gas almost instantaneously owing to the effect of stellar winds neglected in many recent hydrodynamical simulations. We found that if stellar dynamics is suppressed, Type II supernovae (the main source of mechanical feedback) explode in a medium heated and diluted by the stellar winds. In such an environment, radiative losses are small and the supernova feedback is extremely effective. If, on the other hand, stellar motions are allowed, they can move from the natal site (where the gas has been heated and stirred by the effect of stellar winds) to neighboring regions before exploding as supernovae. These regions are characterized by lower temperatures and higher densities, so that the supernova feedback becomes less effective. It is thus crucial to correctly simulate stellar dynamics (together with all relevant sources of feedback) in order to study the interplay between stars and the interstellar medium.

Unlike many other studies of DGs, we used the self-consistent initial gas configuration that was constructed taking the gas self-gravity into account (Vorobyov et al., 2012). This gas configuration is usually more centrally condensed and prone to star formation than that constructed

neglecting gas self-gravity. We compared the evolution of our model galaxy starting from these different initial configurations and found that models that start from non-self-gravitating initial configurations evolve much slower than those that start from self-gravitating ones. In the former, a major episode of star formation and the development of prominent outflows may be delayed by 0.5-0.8 Gyr as compared to the latter. We note that this is exclusively the effect of initial conditions (or, better to say, the effect of using non-self-consistent initial gas configurations), because the gas self-gravity is turned on in both models once the evolution has started.

In the future, a detailed comparison of our stellar hydrodynamics simulations with a more conventional N-body treatment of stellar dynamics is desirable to assess the weak and strong sides of the Boltzmann moment equation approach. This project was partly supported by the Russian Ministry of Education and Science Grant 3.961.2014/K and a Lise Meitner Fellowship, project number M 1255-N16. The simulations were performed on the Vienna Scientific Cluster (VSC-2). This publication is supported by the Austrian Science Fund (FWF). We are thankful to the anonymous referee for a very insightful review which helped to improve the manuscript.

## References

- Bakes, E. L. O., Tielens, A. G. G. M. 1994, *ApJ*, 427, 882
- Black, D. C., Bodenheimer, P. 1975, *ApJ*, 199, 619
- Blondin, J. M., Lufkin, E. A. 1993, *ApJS*, 88, 589
- Böhringer, H. & Hensler, G. 1989, *A&A*, 215, 147
- Burkert, A., & Hensler, G. 1988, *A&A*, 199, 131
- Brook, C. B., Stinson, G., Gibson, B. K., Wadsley, J., & Quinn, T. 2012, *MNRAS*, 424, 1275
- Clarke, D. A. 2010, *ApJS*, 187, 119
- Colella, P., Woodward, P. R. 1984, *J. Comput. Phys.*, 54, 174
- Creasey, P., Theuns, T., & Bower, R. G. 2013, *MNRAS*, 429, 1922
- Dalgarno, A., & McCray, R. A. 1972, *ARA&A*, 10, 375
- Dalla Vecchia, C., & Schaye, J. 2012, *MNRAS*, 426, 130
- Famaey, B., & McGaugh, S. S. 2012, *Living Reviews in Relativity*, 15, 10
- Famaey, B., & McGaugh, S. 2013, *Journal of Physics Conference Series*, 437, 012001
- Freyer, T., Hensler, G., & Yorke, H.W. 2003, *ApJ*, 594, 888
- Genel, S., Vogelsberger, M., Springel, V., et al. 2014, *arXiv:1405.3749*
- Governato, F., Brook, C., Mayer, L., et al. 2010, *Nature*, 463, 203
- Hensler, G. 2007, *EAS Publications Series*, 24, 113
- Hensler, G., & Recchi, S. 2010, *IAU Symposium*, 265, 325
- Hollenbach, D., & McKee, C. F. 1989, *ApJ*, 342, 306
- Hopkins, P. F., Narayanan, D., & Murray, N. 2013, *MNRAS*, 432, 2647
- Hunter, C. 1962, *ApJ*, 136, 594
- Jackson, J. P. 1975, *classical Electrodynamics* (New York: Wiley)
- Katz, N. 1992, *ApJ*, 391, 502
- Kay, S. T., Pearce, F. R., Frenk, C. S., & Jenkins, A. 2002, *MNRAS*, 330, 113
- Kennicutt, R. C. 1998, *ApJ*, 498, 541
- Koeppen, J., Theis, C., & Hensler, G. 1995, *A&A*, 296, 99
- Kroupa, P. 2001, *MNRAS*, 322, 231
- Kroupa, P. 2012, *PASA*, 29, 395
- Kulikov, I. 2014, *ApJS*, 214, 12
- Lasker, B. M. 1967, *ApJ*, 149, 23
- Leitherer, C., Schaerer, D., Goldader, J. D., et al. 1999, *ApJS*, 123, 3
- Lisenfeld, U., Ferrara, A. 1998, *ApJ*, 496, 145
- Mac Low, M.-M., & Ferrara, A. 1999, *ApJ*, 513, 142
- Matteucci, F. 2001, *The chemical evolution of the Milky Way, Astrophysics and Space Science Library*, 253 (Dordrecht: Kluwer Academic Publishers)
- Matteucci, F., Recchi, S. 2011, *ApJ*, 558, 351
- Melioli, C., & de Gouveia Dal Pino, E. M. 2004, *A&A*, 424, 817
- Minchev, I., Chiappini, C., & Martig, M. 2013, *A&A*, 558, A9
- Mitchell, N., Vorobyov, E. I., Hensler, G. 2013, *MNRAS*, 428, 2764

Nomoto, K., Thielemann, F.-K., Yokoi, K. 1984, *ApJ*, 286, 644  
 Norman, M. L., Wilson, J. R., Barton, R. T. 1980, *ApJ*, 239, 968  
 Ostriker, J. P., & Mark, J. W.-K. 1968, *ApJ*, 151, 1075  
 Padovani, P., Matteucci, F. 1993, *ApJ*, 416, 26  
 Perret, V., Renaud, F., Epinat, B., et al. 2014, *A&A*, 562, A1  
 Pilkington, K., Gibson, B. K., Calura, F., et al. 2011, *MNRAS*, 417, 2891  
 Ploekinger, S., Hensler, G., Recchi, S., Mitchell, N., & Kroupa, P. 2014, *MNRAS*, 437, 3980  
 Polyachenko, V. L., Polyachenko, E. V., Strel'nikov, A. V. 1997, *Astron. Z.*, 23, 551 (translated *Astron. Lett.* 23, 483)  
 Recchi, S. 2014, *Advances in Astronomy*, 2014  
 Recchi, S., Calura, F., Kroupa, P. 2009, *A&A*, 499, 711  
 Recchi, S., & Hensler, G. 2013, *A&A*, 551, A41  
 Recchi, S., Matteucci, F., D'Ercole, A. 2001, *MNRAS*, 322, 800  
 Recchi, S., Theis, C., Kroupa, P., & Hensler, G. 2007, *A&A*, 470, L5  
 Renaud, F., Bournaud, F., Emsellem, E., et al. 2013, *MNRAS*, 436, 1836  
 Richtmyer, R. D., & Morton, K. W. 1995, *Difference Methods for Initial Value Problems* (New York: Wiley)  
 Robitaille, T. P., Whitney, B. A. 2010, *ApJ*, 710, 11  
 Roškar, R., Debattista, V. P., & Loebman, S. R. 2013, *MNRAS*, 433, 976  
 Samland, M., Hensler, G., Theis, Ch. 1997, 476, 544  
 Schaye, J., Crain, R. A., Bower, R. G., et al. 2014, *arXiv:1407.7040*  
 Schure, K. M., Kostenko, D., Kaastra, J. S., Keppens, R., Vink, J. 2009, *A&A*, 508, 751  
 Sedov, L. I., 1959, *Similarity and Dimensional Methods in Mechanics*. Academic Press, New York  
 Silich, S. A., & Tenorio-Tagle, G. 1998, *MNRAS*, 299, 249  
 Silich, S., & Tenorio-Tagle, G. 2001, *ApJ*, 552, 91  
 Slyz, A. D. 2007, *EAS Publications Series*, 24, 89  
 Springel, V., Hernquist, L. 2003, *MNRAS*, 339, 289  
 Stinson, G. S., Bovy, J., Rix, H.-W., et al. 2013, *MNRAS*, 436, 625  
 Stinson, G., Seth, A., Katz, N., et al. 2006, *MNRAS*, 373, 1074  
 Stone, J. M., Norman, M. L. 1992, *ApJSS*, 80, 753  
 Stone, J. M., Norman, M. L. 1993, *ApJ*, 413, 198  
 Tasker, E. J. et al. 2008, *MNRAS*, 390, 1267  
 Teyssier, R., Pontzen, A., Dubois, Y., & Read, J. I. 2013, *MNRAS*, 429, 3068  
 Theis, Ch., Burkert, A., Hensler, G. 1992, *A&A*, 265, 465  
 Thornton, K., Gaudlitz, M., Janka, H.-T., & Steinmetz, M. 1998, *ApJ*, 500, 95  
 Tinsley, B. M. 1980, *Fundam. Cosm. Phys.*, 5, 287  
 Truelove, J. K., Klein, R. I., McKee, C. F., et al. 1997, *ApJ*, 489, L179  
 Tomisaka, K. & Ikeuchi, S. 1988 *ApJ*, 330, 695  
 Toomre, A. 1964, *ApJ*, 139, 1217  
 Truelove, K. J., Klein, R. I., McKee, C. F., et al. 1998, *ApJ*, 495, 821  
 Van Dishoeck, E. F., Black, J. H. 1986, *ApJSS*, 62, 109  
 van den Hoek, L. B., & Groenewegen, M. A. T. 1997, *A&AS*, 123, 305  
 Vázquez, G. A., & Leitherer, C. 2005, *ApJ*, 621, 695  
 Vieser, W., & Hensler, G. 2007, *A&A*, 472, 141  
 Vogelsberger, M., Genel, S., Springel, V., et al. 2014, *Nature*, 509, 177  
 von Neumann, J. Richtmyer, R. D. 1950, *J. Appl. Phys.*, 21, 232  
 Vorobyov, E. I., Basu, S. 2005, *A&A*, 431, 451  
 Vorobyov, E. I., Theis, Ch. 2006, *MNRAS*, 373, 194  
 Vorobyov, E. I., Theis, Ch. 2008, *MNRAS*, 383, 817  
 Vorobyov, E. I., Recchi, S., Hensler, G. 2012, *A&A*, 543, 129  
 Vshivkov, V. A., Lazareva, G. G., Snytnikov, A. V., Kulikov, I. M., & Tutukov, A. V. 2011, *ApJS*, 194, 47  
 Weaver, R., McCray, R., Castor, J., et al. 1977, *ApJ*, 218, 177  
 Woosley, S. E., Weaver, T. A. 1995, *ApJS*, 101, 181  
 Zemp, M., Gnedin, O. Y., Gnedin, N. Y., & Kravtsov, A. V. 2012, *ApJ*, 748, 54

## Appendix A: Testing gas hydrodynamics equations

Our numerical scheme for solving the equations of gas hydrodynamics (1)–(4) can be tested using a conventional set of test problems suitable for cylindrical coordinates. Below, we provide the results of six essential test problems, each designed to test the code performance at various physical circumstances. The code has also performed well on two additional tests: the two interacting blast waves and the Noh

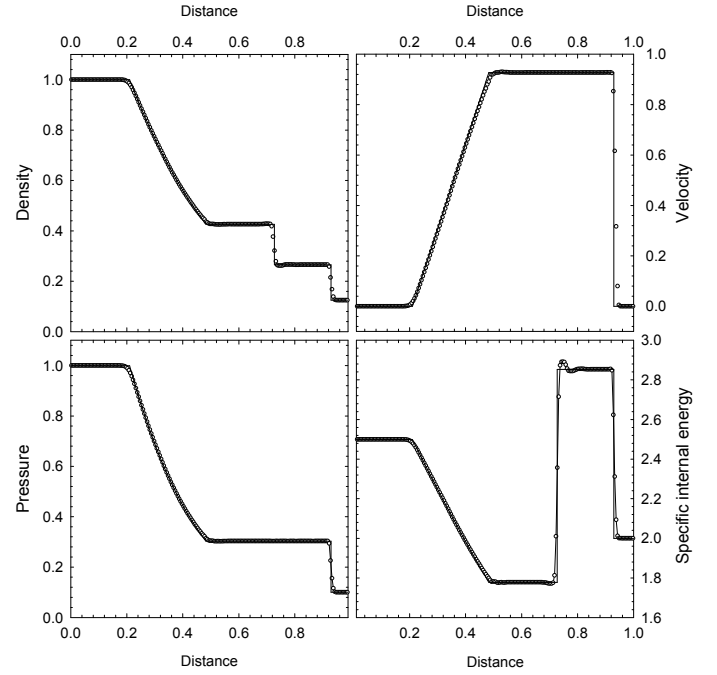


**Fig. A.1.** Sod shock tube problem for the gas density (upper-left), velocity (upper-right), pressure (lower-left), and specific internal energy (lower-right). The numerical solution is shown by open circles, while the analytical one is plotted by solid lines.

(or implosion) problems, but we do not provide the results for the sake of conciseness.

### A.1. Sod shock-tube test

This test is often used to assess the ability of a numerical algorithm to accurately track the position of relatively weak shock waves and contact discontinuities. Initial conditions involve two discontinuous states along the  $z$ -axis, with a hot dense gas on the left and cold rarified gas on the right. More specifically, we set the pressure and density at  $z \in [0 - 0.5]$  to 1.0, while at  $z \in [0.5 - 1.0]$  the pressure is 0.1 and density is 0.125. The velocity of a  $\gamma = 1.4$  gas is initially zero everywhere.

Filled circles in Figure A.1 show the results of the Sod shock-tube test computed with a resolution of 200 grid zones and  $C_2 = 4$  (the number of zones over which the shock is spread), while the solid lines plot the analytic solution at  $t = 0.235$ . It is evident that the code tracks well the positions of shock waves and contact discontinuities, which are resolved by 3–4 zones, in accordance with the chosen value of  $C_2$ . Decreasing  $C_2$  results in sharper shocks and contact discontinuities but may increase the magnitude of anomalous spikes in the specific energy (bottom-right panel), and hence not recommended. Increasing  $C_2$  to 6 produces results similar to those for  $C_2 = 4$ , except that the shocks and contact discontinuities are now resolved by 5–6 zones.

### A.2. Sedov point explosion

The Sedov explosion problem tests the code's ability to deal with strong shocks. In contrast to the Sod shock-tube test, in which shock waves were of a pure planar geometry, this

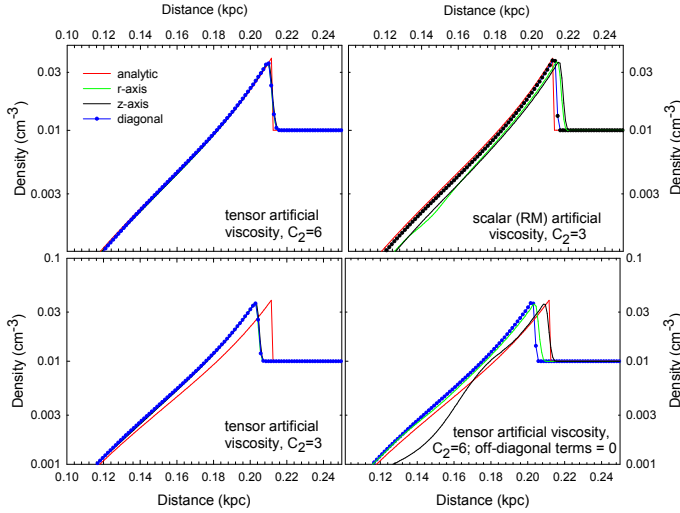


**Fig. A.2.** Sedov point explosion test for the explosion energy  $10^{51}$  erg and background density  $n = 0.01 \text{ cm}^{-3}$ . The analytic solution is shown by the red lines, while the numerical solutions along the  $z$ -axis,  $r$ -axis, and diagonal  $z = r$  are shown by the black, pink, and blue lines, respectively. The top-left panel presents the solution for the tensor artificial viscosity with  $C_2 = 6$ , the top-right panel—for the scalar artificial viscosity and  $C_2=3$ , the bottom-left panel—for the tensor artificial viscosity and  $C_2 = 3$ , and the bottom-right panel—for the tensor artificial viscosity with zero off-diagonal terms and  $C_2=6$ .

test involves a spherically symmetric strong shock wave. Hence, the point explosion is a powerful test on the code’s ability to render spherically symmetric structures on an essentially non-spherical grid stencil.

To initialize the explosion, we consider a cold ( $T = 10 \text{ K}$ ) homogeneous medium with number density  $n = 10^{-2} \text{ cm}^{-3}$  and inject  $10^{51}$  ergs of thermal energy (equivalent to one supernova) into the innermost grid cell. The adopted resolution is  $300 \times 300$  grid cells and the size of each cell is  $1.0 \text{ pc}$  in each coordinate direction ( $z$  and  $r$ ). We emphasize that we do not inject energy into a central sphere comprising a few cells near the coordinate origin—a usual practice to alleviate the problem of a non-spherical geometry. Instead, we consider the most difficult situation when energy is injected in just one, essentially cylindrical innermost cell.

Figure A.2 compares our derived density distributions along the  $z$ -axis (black line), the  $r$ -axis (pink line), and the diagonal  $z = r$  (blue line with circles) with the analytic solution given by the red line (Sedov, 1959) at  $t=1 \text{ Myr}$  after the explosion. In particular, numerical simulations in the top-left panel are obtained using the tensor artificial viscosity (AV) as defined in Section 4, while the density distribution in the top-right panel is obtained using the “classic” scalar AV as described by Richtmyer & Morton (1995). It is evident that the tensor AV yields a much better agreement with the analytic solution. The expanding shell has almost a perfect spherical shape (all three lines showing the numerical solution virtually coincide), notwithstanding the fact that the energy was injected into a cylindrically shaped innermost cell. On the other hand, the Richtmyer & Morton scalar AV yields a notable deviation from sphericity along the  $r$  and  $z$  axes, as seen in the top-right panel of

Figure A.2. The Richtmyer & Morton solution also slightly overshoots the analytical one. Regardless of the AV prescription used, the shock front is resolved by 2–3 grid zones.

We want to emphasize that all components of the artificial viscosity tensor  $\mathbf{Q}$  should be used, including the off-diagonal terms. Neglecting the latter, as is done in, e.g., Stone & Norman (1992), leads to a significant deterioration of the numerical solution. The bottom-right panel in Figure A.2 demonstrates the effect of zeroing the off-diagonal terms in  $\mathbf{Q}$ . As one can see, the numerical solution is skewed, notably undershooting the position of the shock front in the  $r$ -direction and along the diagonal direction but reproducing the shock front rather well in the  $z$ -direction.

A caution should be paid when choosing the AV softener  $C_2$ . As one can notice in Figure A.2, the test was done with different values of  $C_2$  for the tensor and scalar AV, 6 and 3, respectively. If we choose  $C_2 = 3$  for the tensor AV, the position of the shock front notably undershoots the analytic solution, as is illustrated in the bottom-left panel of Fig. A.2. Fortunately, once the proper value of  $C_2$  is found, the tensor AV algorithm performs well regardless of the energy input, background density, or numerical resolution. We demonstrate this in Figure A.3 showing the tensor AV performance for various choices of the input parameters as indicated in each panel and  $C_2 = 6$ . It is evident that the test results are virtually insensitive to a particular choice of initial conditions.

The sensitivity of the Sedov test to a particular choice of the AV softener  $C_2$  is a well known problem of numerical codes that evolve the internal energy (e.g. Tasker et al., 2008). Switching to the total energy helps to eliminate this problem (e.g. Clarke, 2010). However, in numerical codes that make use of a staggered grid as our own, with vector and scalar variables defined at different positions on the grid, solving for the total energy equation is not a good option as it inevitably requires interpolating between the internal and kinetic energies to obtain the total one (Clarke, 2010) or applying corrections after each time step to conserve the total energy (Vshivkov et al., 2011). In either case, this practice, according to our experience, often comes at a cost of degraded performance on other test problems and is not recommended. Instead, we show that a proper choice of the artificial viscosity softener can help to resolve this problem without resorting to the total energy equation.

### A.3. Collapse of a pressure-free sphere

The gravitational collapse of a pressure-free sphere is used to assess the code’s ability to accurately treat converging spherical flows in cylindrical coordinates. This test is also useful for estimating the performance of the gravitational potential solver on dynamical problems (our solver does well on the static configurations such as spheres and ellipsoids). To run this test, we set a cold homogeneous sphere of unit radius and density (for convenience, the gravitational constant is also set to unity) and let it collapse under its own gravity. The analytic solution to this problem exists only in the limit of an infinite cloud radius, describing the collapse of every mass shell (Hunter, 1962). In the cylindrical geometry, however, we consider a cloud of finite radius with a sharp outer boundary to preserve the cloud sphericity. As a result, a rarefaction wave develops after the onset of the collapse, propagating towards the coordinate origin



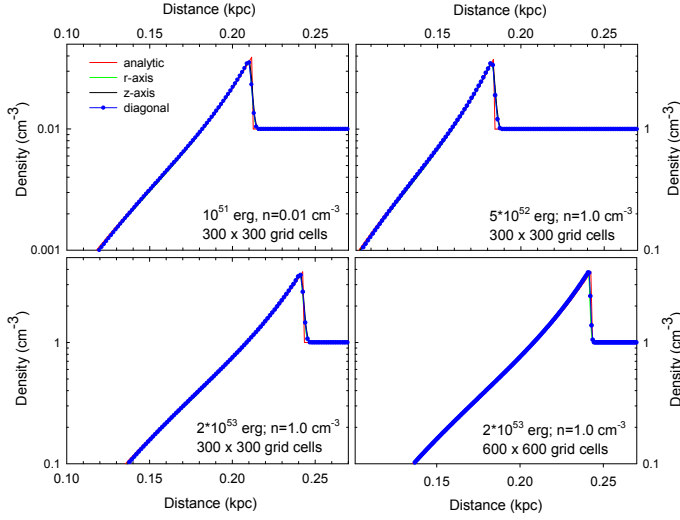


**Fig. A.3.** Sedov point explosion test for various explosion energies, background densities and numerical resolutions as indicated in each panel. The tensor artificial viscosity with  $C_2 = 6$  is used for every plot. The line meaning is the same as in Figure A.2.

and necessitating complicated corrections to the analytic solution (Truelove et al., 1998).

The left panel in Figure A.4 compares the results of our numerical simulations with the “uncorrected” analytic solution of Hunter (1962) (red line) at  $t=0.535$  (or  $0.985$  that of the free-fall time) when the initial density has increased by nearly three orders of magnitude. As in the previous test, we plot the numerically derived density along the  $z$ -axis (black line),  $r$ -axis (green line), and the  $z = r$  diagonal (blue line with circles). The numerical resolution is  $200 \times 200$  grid zones. It is seen that the cloud’s outer boundary is somewhat smeared out due to the action of the rarefaction wave. The peak density is also about 1% smaller than that predicted from the analytic solution. On the other hand, the code performs well on preserving sphericity of the collapsing cloud. In the right panel, we turn off the volume averaging corrections applied to the advection of the  $r$ -momentum in the  $r$ -direction (as described in Blondin & Lufkin (1993)), which results in the development of an artificial density spike near the  $z$ -axis and also in the distortion of a spherically symmetric collapse. This test demonstrates the utility of the volume averaging corrections introduced originally by Blondin & Lufkin (1993) in the PPA advection scheme in non-Cartesian coordinates.

#### A.4. Collapse of a rotating sphere

This test is invoked to assess the code’s ability to conserve angular momentum. The setup consists of a isothermal ( $T=10$  K) homogeneous sphere of unit radius and density, which rotates at a constant angular velocity  $\Omega_0$ . The latter is found from the requirement that the ratio  $\beta$  of the rotational energy  $E_{\text{rot}} = I\Omega_0^2/2$  to gravitational energy  $E_{\text{grav}} = 3GM_0^2/(5R)$  is equal to 5%. Here,  $I = 2M_0R^2/5$  is the moment of inertia of a homogeneous sphere of radius  $R$  and mass  $M_0$ . The adopted value of  $\beta = 0.05$  is close to an upper limit found in rotating pre-stellar molecular cloud cores and dark matter halos.

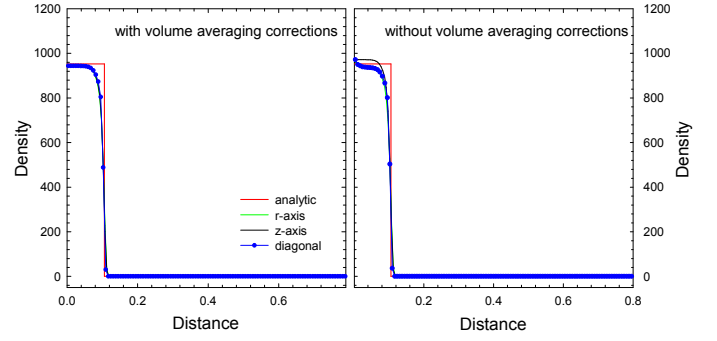


**Fig. A.4.** Collapse of a pressure-free sphere showing the gas density at  $0.985$  that of the free-fall time. The left/right panels show the test results with/without the volume averaging corrections as described in Blondin & Lufkin (1993). The line meaning is the same as in Figure A.2.

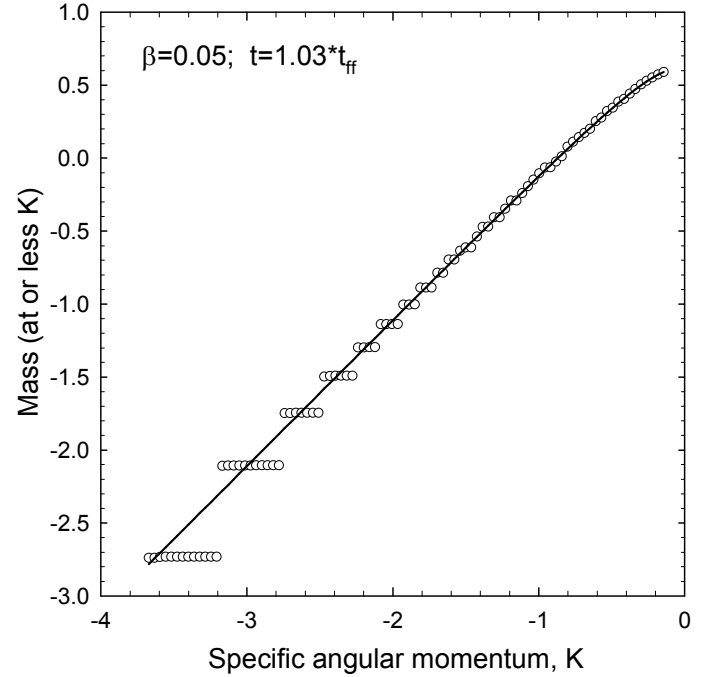


**Fig. A.5.** Specific angular momentum spectrum  $M(K)$ , calculated using equation (A.1), for a collapsing sphere at  $1.03t_{\text{ff}}$ . The analytic spectrum is shown by the solid line, while the test results are plotted by open circles.

In the absence of any mechanisms for angular momentum redistribution, the mass with specific angular momentum less than or equal to  $K = \omega r^2$ , where  $\omega$  is the angular velocity at a distance  $r$  from the  $z$ -axis, should be conserved and equal to (Norman et al., 1980)

$$M(K) = M_0 \left[ 1 - \left( 1 - \frac{K}{\Omega_0 R^2} \right)^{3/2} \right]. \quad (\text{A.1})$$

A deviation from equation (A.1) would manifest the non-conservation of angular momentum in the numerical algorithm.

The solid line in Figure A.5 shows the initial mass spectrum  $M(K)$ , whereas the open circles present the mass spectrum obtained at time  $1.03 \times t_{\text{ff}} = 0.551$ , where  $t_{\text{ff}}$  is the free-fall time for a non-rotating sphere of the same density and radius. The numerical resolution is  $200 \times 200$  grid zones.



By  $t = 0.551$ , the density near the center of the sphere has increased by more than three orders of magnitude, but the deviation of the mass spectrum from the initial configuration is negligible everywhere except at lowest values of  $K$ . This deviation is a manifestation of angular momentum non-conservation near the rotational axis caused by imperfections in the interpolation procedure across the inner  $r$ -boundary. Nevertheless, the total mass of gas that suffers from the angular momentum non-conservation is just below 1% and therefore should not affect notably the global evolution.

#### A.5. Kelvin-Helmholtz Instability

The Kelvin-Helmholtz instability (KHI) occurs at the interface between two fluid moving with different velocities. In the context of this paper, this instability operates at the interface between the hot supernova ejecta and the cold swept-up shell and may cause an accelerated disintegration of the latter (e.g. Vorobyov & Basu, 2005). Therefore, it is essential that the code be able to demonstrate the development of the KHI as expected from the linear perturbation theory.

The initial setup involves two fluids moving in opposite directions along the  $z$ -axis with the relative velocity  $v_{z,\text{rel}} = 0.2c_s$ , where  $c_s = 0.06$  is the sound speed. The interface between the fluids is located at  $r = 0.5$  and the densities of the inner and outer fluids are  $\rho_{\text{in}} = 1.0$  and  $\rho_{\text{out}} = 0.1$ , respectively. We use periodic boundary conditions and the resolution is  $200 \times 200$  grid zones on the  $1.0 \times 1.0$  computational domain.

To trigger the instability, we impose a sinusoidal perturbation on the radial velocity  $v_r$  of the form

$$v_r = \delta v_r \sin(2\pi z/\lambda), \quad (\text{A.2})$$

where the amplitude and wavelength of the perturbation are  $\delta v_r = v_{z,\text{rel}}/100$  and  $\lambda = 1/6$ , respectively. The perturbation is applied to five neighboring grid zones on both sides of the fluid interface.

Figure A.6 demonstrates the growth of the KHI with time. There are six growing vortices, in agreement with the wavelength of the perturbation  $\lambda = 1/6$ , and the growth time is approximately 50–60, again in agreement with the characteristic growth time of the KHI for our choice of the fluid density and velocity

$$\tau_{\text{KH}} = \frac{\lambda(\rho_{\text{in}} + \rho_{\text{out}})}{v_{z,\text{rel}}\sqrt{\rho_{\text{in}}\rho_{\text{out}}}} = 48.3. \quad (\text{A.3})$$

We should note here that, for this particular test, gravity can be neglected. Therefore, all modes of perturbation, irrespective of their wavelengths (or wavenumbers) are unstable (see Vieser & Hensler, 2007, for stability criteria when gravity is taken into account).

#### A.6. Overstability of a radiative shock

A useful test problem for hydrodynamic codes with optically thin radiative cooling is described in Stone & Norman (1993). The test involves setting a uniform flow of gas with velocity  $v_0$  against a reflecting wall. An adiabatic reflection shocks forms immediately at the wall and propagates upstream with velocity  $v_{\text{sh}} = v_0/3$ . After approximately one cooling time, the shock loses its pressure support and is

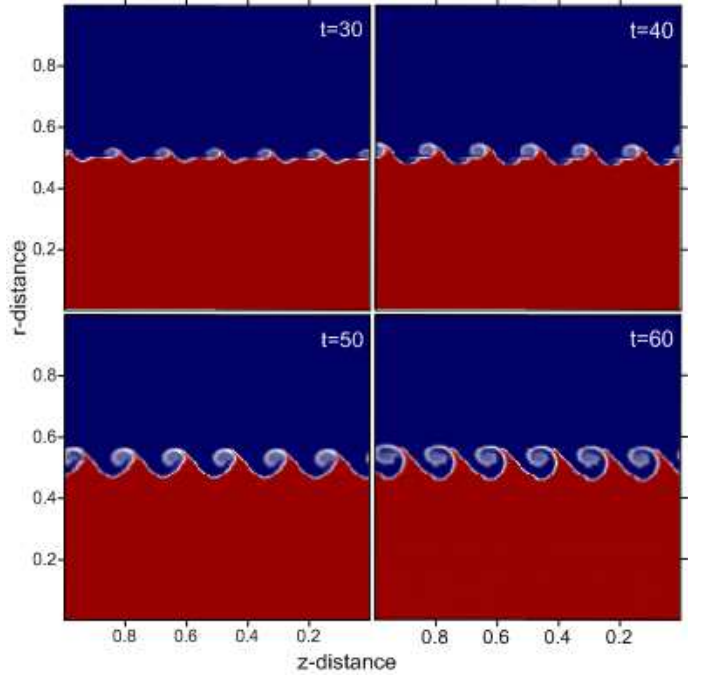


**Fig. A.6.** Development of the KHI at different moments in time (see text for more detail).

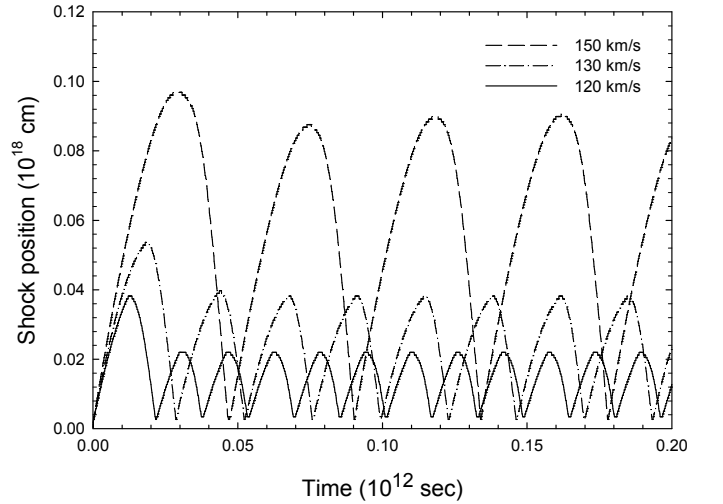


**Fig. A.7.** Shock position versus time of a one-dimensional radiative shock during overstable oscillations. The shock positions for the flow velocities of  $120 \text{ km s}^{-1}$ ,  $130 \text{ km s}^{-1}$  and  $150 \text{ km s}^{-1}$  are plotted with solid, dash-dotted, and dotted lines, respectively.

then advected back to the wall at  $v_{\text{sh}} \lesssim -v_0$ . After reflecting off the wall, the shock again becomes adiabatic and propagates outward to repeat the cycle.

Figure A.7 presents the test results for the cooling function with solar metallicity and ionization fraction  $f_{\text{ion}} = 10^{-3}$ . Gas heating is turned off for this test. The initial setup is identical to that described in Stone & Norman (1993), i.e., the initial gas number density and temperature are set to  $10 \text{ cm}^{-3}$  and  $10^4 \text{ K}$ , respectively. The position of the shock front for three flow velocities of  $120 \text{ km s}^{-1}$ ,  $130 \text{ km s}^{-1}$  and  $150 \text{ km s}^{-1}$  are plotted with the solid, dash-dotted, and dashed lines, respectively. The shock position demonstrates regular pulses, as expected. The ampli-

tude and period of the observed oscillations are somewhat different from those presented in Stone & Norman (1993), which simply reflect the difference in the adopted cooling functions. The upstream velocity of the adiabatic shock is close to the expected value,  $v_0/3$ . For instance, in the case of  $v_0 = 150 \text{ km s}^{-1}$ , the maximum upstream velocity of the shock is  $47 \text{ km s}^{-1}$ . This test demonstrates the reliability of our solution scheme for the gas cooling and heating described in Section 3.

## Appendix B: Testing stellar hydrodynamics equations

Testing the stellar hydrodynamics equations (6)–(8) presents a certain challenge since stellar systems are described by a stellar dispersion tensor, which may be anisotropic, rather than by an isotropic pressure. Fortunately, some of the test problems considered above can be adapted to stellar hydrodynamics as well. The matter is that the equations of stellar hydrodynamics can be formally made identical to those of gas hydrodynamics for a specific set of initial conditions (note that the continuity equations are always identical). Indeed, for a one dimensional flow along the  $z$ -direction (with zero gravity and no star formation), equations (7) and (8) become

$$\frac{\partial}{\partial t} (\rho_s v_{s,z}) + \frac{\partial}{\partial z} (\rho_s v_{s,z} \cdot v_{s,z}) + \frac{\partial}{\partial z} (\rho_s \sigma_{zz}^2) = 0, \quad (\text{B.1})$$

$$\frac{\partial}{\partial t} (\rho_s \sigma_{zz}^2) + \frac{\partial}{\partial z} (\rho_s \sigma_{zz}^2 \cdot v_{s,z}) + 2\rho_s \sigma_{zz}^2 \frac{\partial v_{s,z}}{\partial z} = 0. \quad (\text{B.2})$$

These equations become identical to the corresponding gas dynamics equations for  $\rho_g v_z$  and  $\epsilon$ , if we set  $\rho_s \sigma_{zz}^2 = P$ ,  $\epsilon = (\gamma - 1)\rho_s \sigma_{zz}^2$ , and  $\gamma = 3$  (see Mitchell et al., 2013, for details). This fact allows us to directly compare the performance of both stellar and gas hydrodynamics code on some test problems considered in Section A or use analytic solutions available from the gas dynamics.

### B.1. Sod shock-tube test

The initial setup for this test is identical to that considered in Section A.1. We run the test along the  $z$ -axis and set  $\rho_s \sigma_{zz}^2$  and  $\rho_s$  at  $z \in [0 - 0.5]$  to 1.0, while at  $z \in [0.5 - 1.0]$  the  $z$ -component of the stress tensor is 0.1 and stellar density is 0.125.

Our numerical results for  $C_{2s} = 4$  and  $t = 0.14$  (open circles) are compared against the analytical solution (solid lines) in Figure B.1. It is seen that our numerical scheme correctly reproduces the position of shock waves and contact discontinuities in the stellar fluid. On the other hand, small-scale oscillations are evident at shock positions, perhaps reflecting the lack of energy dissipation due to the collisionless nature of stellar hydrodynamics. An increase in the coefficient of artificial viscosity helps to reduce the amplitude of spurious oscillations but simultaneously increases the shock smearing and hence is recommended only if these oscillations lead to numerical instabilities.

### B.2. Collapse of a cold sphere and angular momentum conservation

The collapse of a cold stellar sphere, both with and without rotation, have produces very similar results to those of

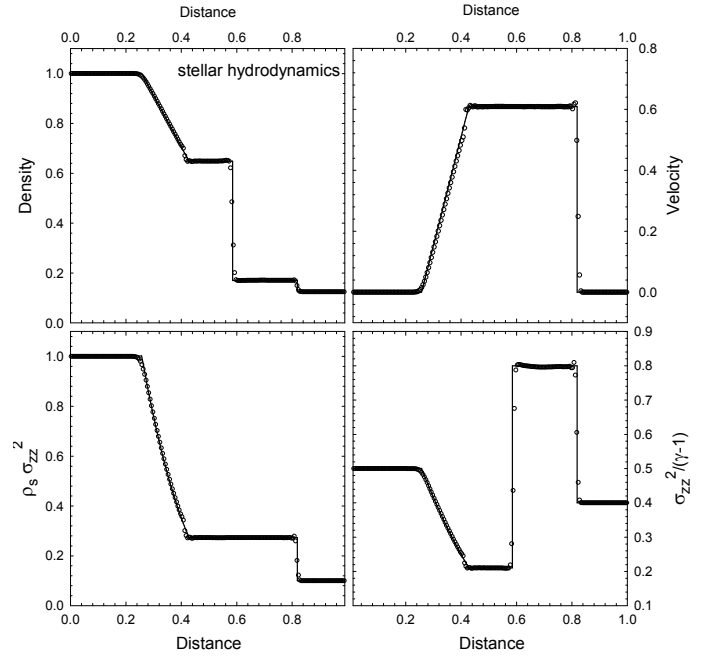


**Fig. B.1.** Sod shock tube problem for the stellar density (upper-left), velocity (upper-right),  $z$ -component of the stress tensor (lower-left), and square of the  $z$ -velocity dispersion (lower-right). The numerical solution is shown by open circles, while the analytical one is plotted by solid lines.

presented in Sections A.3 and A.4 and will not be repeated here. This ensures that our stellar hydrodynamics part is expected to perform well on problems involving gravitational contraction/expansion with and without rotation.

## Appendix C: Testing the chemical evolution routines

Nowadays it is common to find hydrodynamical codes coupled with passive scalars (or other numerical techniques), able to follow the evolution of the metals in a simulation. However, usually no test is performed to check the numerical accuracy of these routines. Actually, since a very vast literature on analytical solutions of the chemical evolution of galaxies and other astronomical objects exists (see e.g. Tinsley, 1980; Matteucci, 2001; Hensler & Recchi, 2010, and references therein) it is indeed not difficult to benchmark the chemical evolution routines of a chemodynamical code.

The “closed box” model of chemical evolution is based on the following assumptions: (i) the system is uniform and closed (there are no inflows or outflows), (ii) the IMF does not change with time, (iii) the gas is well mixed at any time and (iv) stars more massive than a certain threshold mass  $M_{thr}$  die instantaneously whereas stars less massive than  $M_{thr}$  live forever. This last assumption, although very restrictive, is fulfilled if we look at specific chemical elements, in particular O and the other  $\alpha$ -elements, since they are mostly synthesized by Type II SNe and the (long-living) low- and intermediate-mass stars contribute negligibly to their production.

In a system made up of only gas and stars (DM does not play any role here) we define the quantities

$$R = \int_{M_{thr}}^{\infty} [M - M_{rem}(M)] \phi(M) dM, \quad (C.1)$$

$$y_O = \frac{1}{1 - R} \int_{M_{thr}}^{\infty} M p_O(M) \phi(M) dM, \quad (C.2)$$

where  $M_{tot} = M_{gas} + M_{stars}$ ,  $M_{rem}(M)$  is the remnant mass after a star of mass  $M$  has died and  $M p_O(M)$  is the oxygen mass newly synthesized by the star of mass  $M$  ( $p_O(M)$  is the true yield of O). Under the initial condition  $M_{gas} f(0) = Const. = M_{tot}$ ,  $M_{stars}(0) = 0$ ,  $X_O(0) = X_0$  it is not difficult to find that

$$X_O = \frac{M_O}{M_{gas}} = X_0 + y_O \ln(\mu^{-1}), \quad (C.3)$$

where  $\mu = M_{gas}/M_{tot}$ . This is the famous analytical solution of the closed box model, which depends only on the gas fraction  $\mu$ .

We have integrated numerically eqs. C.1 and C.2 by using the values of  $M_{rem}(M)$  and  $M p_O(M)$  tabulated by Woosley & Weaver (1995), using  $Z=0.01 Z_{\odot}$  as initial metallicity. We do not use  $Z=0$  as initial metallicity for two reasons: firstly, for  $Z(0)=0$  the cooling is very low and the resulting star formation is too weak; secondly, the yields  $p_O(M)$  tabulated by Woosley & Weaver (1995) at this metallicity oscillate considerably and that makes the calculation of  $y_O$  by means of Eq. C.2 less accurate. By properly choosing a reference volume in the computational box (namely a volume encompassing all the metals produced and advected within a time span of 100 Myr) we can thus calculate the variation of  $\mu$  with time and, from it, the analytical evolution of the oxygen mass fraction  $X_O$  with time. This is plotted in Fig. C.1 (solid line), together with the direct numerical calculation of  $M_O/M_{gas}$ , averaged over the same volume (dashed line). The two curves converge only after  $\sim 30$  Myr. This is expected because we have to ensure that Type II SNe of all initial masses contribute to the production of O and  $\sim 30$  Myr is approximately the lifetime of the less massive SNeII. After a time of  $\sim 40$  Myr the two curves almost overlap, demonstrating that our chemical routines are able to accurately follow the overall chemical evolution of a galaxy.

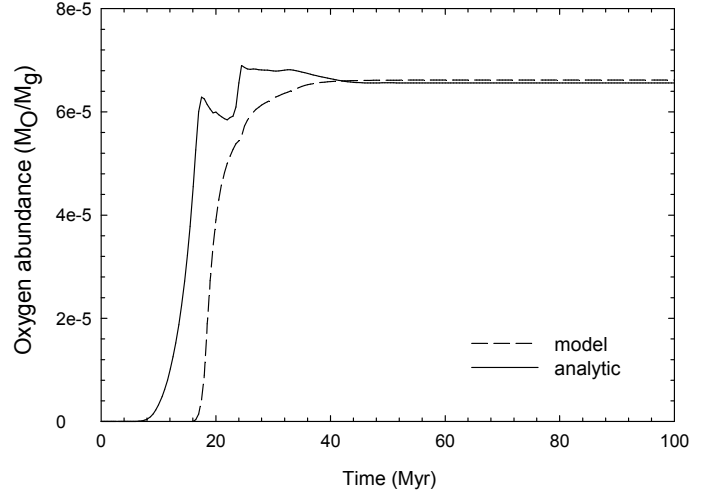


**Fig. C.1.** The evolution with time of the mass fraction of oxygen as derived from the analytical expression Eq. C.3 (solid line) and from our numerical simulation (dashed line). See text for more detail.